MAVEN/IUVS Stellar Occultation Measurements of Mars Atmospheric Structure and Composition

Journal of Geophysical Research: Planets

RESEARCH ARTICLE
10.1029/2017JE005466

MAVEN/IUVS Stellar Occultation Measurements of Mars Atmospheric Structure and Composition

H. Gröller[1], F. Montmessin[2], R. V. Yelle[1], F. Lefèvre[2], F. Forget[3], N. M. Schneider[4], T. T. Koskinen[1], J. Deighan[4], and S. K. Jain[4]

[1]Lunar and Planetary Laboratory, University of Arizona, Tucson, AZ, USA, [2]Guyancourt, LATMOS, Université Versailles Saint-Quentin/CNRS, France, [3]Laboratorie de Météorologie Dynamique, Institute Pierre-Simon Laplace, Paris, France, [4]Laboratory for Atmospheric and Space Physics, University of Colorado Boulder, Boulder, CO, USA

Key Points:
- The execution of MAVEN/IUVS stellar occultation campaigns and the retrieval process to infer physical quantities are described in detail
- Distribution of molecular oxygen and ozone is measured
- Highly structured atmospheric perturbations are interpreted as atmospheric tides

Correspondence to:
H. Gröller,
hgr@lpl.arizona.edu

Citation:
Gröller, H., Montmessin, F., Yelle, R. V., Lefèvre, F., Forget, F., Schneider, N. M., et al. (2018). MAVEN/IUVS stellar occultation measurements of Mars atmospheric structure and composition. *Journal of Geophysical Research: Planets*, *123*, 1449–1483. https://doi.org/10.1029/2017JE005466

Received 11 OCT 2017
Accepted 29 APR 2018
Accepted article online 21 MAY 2018
Published online 14 JUN 2018

Abstract The Imaging UltraViolet Spectrograph (IUVS) instrument of the Mars Atmosphere and Volatile EvolutioN (MAVEN) mission has acquired data on Mars for more than one Martian year. During this time, beginning with March 2015, hundreds of stellar occultations have been observed, in 12 dedicated occultation campaigns, executed on average every 2 to 3 months. The occultations cover the latitudes from 80°S to 75°N and the full range longitude and local times with relatively sparse sampling. From these measurements we retrieve CO_2, O_2, and O_3 number densities as well as temperature profiles in the altitude range from 20 to 160 km, covering 8 orders of magnitude in pressure from $\sim 2 \times 10^1$ to $\sim 4 \times 10^{-7}$ Pa. These data constrain the composition and thermal structure of the atmosphere. The O_2 mixing ratios retrieved during this study show a high variability from 1.5×10^{-3} to 6×10^{-3}; however, the mean value seems to be constant with solar longitude. We detect ozone between 20 and 60 km. In many profiles there is a well-defined peak between 30 and 40 km with a maximum density of $1-2 \times 10^9$ cm^{-3}. Examination of the vertical temperature profiles reveals substantial disagreement with models, with observed temperatures both warmer and colder than predicted. Examination of the altitude profiles of density perturbations and their variation with longitude shows structured atmospheric perturbations at altitudes above 100 km that are likely nonmigrating tides. These perturbations are dominated by zonal wave numbers 2 and 3 with amplitudes greater than 45%.

1. Introduction

The Mars Atmosphere and Volatile EvolutioN (MAVEN) mission is designed to study the structure and escape of the Martian atmosphere, and therefore, MAVEN measurements focus on the upper atmosphere and induced magnetosphere of Mars (Jakosky et al., 2015). To fully understand the escape of the atmosphere also requires knowledge of the lower atmosphere because the physical state of the upper atmosphere depends strongly on conditions in the lower atmosphere. The amount of vertical mixing in the atmosphere, especially in the transition region from the middle atmosphere to the upper atmosphere, determines the abundance of minor species and isotopes in the upper atmosphere, thereby affecting the loss of these species over time (Jakosky et al., 2017). Moreover, temperatures in the upper atmosphere depend on the thermal structure of the lower atmosphere through thermal conduction and radiative transfer in the CO_2 15-μm band, which connect the two regions. MAVEN houses an array of instruments (Mass Spectrometer, Ion Spectrometers, Electron Spectrometer, Magnetometer, Langmuir Probe and Wave Instrument, and Accelerometer) that measure the upper atmosphere in situ. Typical orbits penetrate the Martian atmosphere to ~150 km, while targeted Deep Dip campaigns probe the atmosphere to altitudes of 125–130 km, essentially the base of the thermosphere. Still, as discussed above, there is a need to understand the connection of the upper atmosphere to the lower atmosphere: this is provided by the Imaging UltraViolet Spectrograph (IUVS).

The IUVS instrument operates in the far ultraviolet (FUV) and mid-ultraviolet (MUV) wavelength ranges and measures atmospheric emissions from ~50 to 130 km and atmospheric transmission from ~20 to 160 km. Stellar occultations measure transmission by monitoring the spectrum as the motion of the spacecraft carries the line of sight (LOS) from the spectrograph to the star through the atmosphere. The atmospheric transmission is the ratio of the attenuated spectra to an unattenuated spectrum of the star. These transmission spectra are used to infer the density profile of molecular species according to their distinctive absorption features.

Occultation experiments have several virtues. Atmospheric properties are inferred from relative measurements, and analysis of occultations is independent of uncertainties in absolute calibration. Moreover, good altitude sampling can be obtained for bright stars because the resolution is limited by the sampling rate rather than the angular size of the entrance slit. Finally, because absorption cross sections vary strongly with wavelength, a large-altitude region can be studied; thus, the IUVS occultations encompass both the upper and lower atmosphere.

UV occultation observations were used to probe the Martian atmosphere by the Spectroscopy for Investigation of Characteristics of the Atmosphere of Mars (SPICAM) experiment on board of Mars Express (MEX) (Forget et al., 2009; Montmessin, Bertaux, et al., 2006; Montmessin, Quémerais, et al., 2006; Quémerais et al., 2006; Sandel et al., 2015). The MAVEN occultation investigation is based partly on the SPICAM experience. Both SPICAM and IUVS occultations provide CO_2, O_2, and O_3 densities, aerosol opacity, and thermal structure. SPICAM stellar occultations provided the first detection of condensation clouds in the Mars middle atmosphere (Montmessin, Bertaux, et al., 2006), the first altitude profiles of O_3 (Lebonnois et al., 2006), the climatology of the middle and upper atmosphere (Forget et al., 2009), the characterization of tides in the middle atmosphere (Withers et al., 2011), and the first direct measurement of O_2 in the upper atmosphere (Sandel et al., 2015).

Though similar in function, the MEX/SPICAM and MAVEN/IUVS occultation experiments differ in a number of ways. IUVS measures the 110- to 340-nm region in two channels, the FUV from 110 to 190 nm and the MUV from 180 to 340 nm (McClintock et al., 2015), whereas SPICAM used one channel to cover both ranges. The use of two channels provides higher sensitivity and spectral resolution but with added complexity and the burden to join together the FUV and MUV in a seamless fashion. SPICAM occultations were limited mostly to the nightside because of stray light levels on the dayside. Though stray light is often a serious problem for IUVS, we have nevertheless been able to obtain many successful dayside occultations. Finally, continued development of the occultation analysis tools has allowed us to make some improvements in our techniques that significantly benefit the analysis of the IUVS data. As described in the following pages, the IUVS occultation observations confirm many of the SPICAM discoveries and continue the characterization of climatology. This latter point is important because the Martian atmosphere is highly variable on numerous time scales (daily, seasonally, and yearly), and measurements simultaneous with the in situ observations are necessary to understand the variability and its consequences.

This paper provides an overview of results of UV stellar occultations executed with the MAVEN/IUVS instrument. We also describe the specifications of the IUVS instrument for stellar occultations and explain the design and the execution of IUVS stellar occultation campaigns. Furthermore, we provide a detailed description of the data reduction and analysis procedures needed to retrieve number densities and temperature profiles from the measurements including the errors and uncertainties associated with each step of the analysis procedures. We present a subset of scientific results that can be obtained from UV stellar occultations in order to clearly illustrate the harvest from this experiment and the quality of the data. These include altitude profiles and geographic and temporal variability of CO_2, O_2, and O_3 densities, characteristics of vertical temperature profiles, and evidence for tidal signatures in the upper atmosphere.

2. MAVEN/IUVS Stellar Occultations

The IUVS is located on MAVEN's Articulated Payload Platform (APP). The spacecraft and APP maintain inertial pointing during an occultation to obtain an uninterrupted record of the stellar signal transmitted through the Mars atmosphere. The starlight enters the spectrograph through one of two square areas at the ends of the IUVS entrance slit (referred to as "keyholes") and is dispersed by the grating into first and second diffraction orders with wavelengths of 110–190 and 180–340 nm, respectively. A beam splitter transmits wavelengths greater than 180 nm to the MUV detector and reflects wavelengths less than than 180 nm to the FUV detector. The keyholes are included in the IUVS design because the large angular size is needed to ensure star acquisition given the spacecraft pointing accuracy. The large keyhole has a field of view of 0.69° by 0.90° and the small keyhole has a field of view of 0.29° by 0.40° (McClintock et al., 2015). The first occultations were performed with the large keyhole, but it was discovered that the MAVEN spacecraft has excellent stability and pointing accuracy and the small keyhole has been used for subsequent occultation observations. A more detailed description of the IUVS instrument and the technical specifications can be found in McClintock et al. (2015).

The IUVS data are binned in both the dispersion (spectral) and cross dispersion (spatial) directions in order to reduce data volume. Spectral binning is based on the properties of the line spread function, which is approximately Gaussian with a full width at half maximum of 0.6 and 1.2 nm for the FUV and the MUV channels, respectively (McClintock et al., 2015). The spectral width of an MUV pixel is 0.1654 nm. The spectral width of the FUV pixels depends on the illumination geometry, varying with increasing spectral pixel number from 0.0824 to 0.0799 nm for observations in the large keyhole and from 0.0809 to 0.0829 nm for observations in the small keyhole. The maximum sampling is thus roughly seven samples per spectral resolution element. For the first stellar occultations executed in March 2015, four spectral pixels are binned, resulting in an effective sampling of 0.3296–0.3195 and 0.6614 nm for the FUV and the MUV channels, respectively. For all subsequent occultations three spectral pixels are binned, producing an effective sampling of 0.2426–0.2488 for FUV and 0.49605 nm for MUV. This spectral binning provides better than Nyquist sampling of the spectra. Six pixels are binned in the spatial direction. The stellar signal is concentrated in the 1 or 2 central lines comprised from these bins, but 20 lines are returned in order to characterize stray light and background levels. The occultation frames, consisting of these 20 lines of spectra each with 256 or 341 spectral samples, are recorded at a cadence between 1.6 and 5.6 s consisting of a 1- to 5-s integration time, depending on the star, and 0.6 s of overhead (detector readout, etc.).

Occultations are executed in dedicated campaigns that last between 1 and 2 days. Each campaign consists of occultation measurements using a small set (8–14) of stars that can be observed during a single MAVEN orbit. The sequence of observations is repeated every orbit during the campaign. Campaigns 1–9 consisted of 5 consecutive orbits but this was increased to 10 consecutive orbits beginning with campaign 10. Repeated measurements of a particular star provide measurements at essentially constant latitudes and local times but different longitudes. A campaign of five consecutive orbits covers roughly one planetary rotation and thus provides complete longitudinal coverage: 10 consecutive orbits produces denser longitude sampling. Campaign design is an intensive process. For each campaign, an algorithm is used to find the list of potential target stars based on star brightness and coverage in latitude and local time, while respecting the prohibited regions for instrument and APP pointing and the spacecraft slew rate. The stars are chosen from a catalog of well-characterized UV bright stars. A description of the UV star catalog is given in Appendix A. Our algorithm delivers several possible lists from which one is chosen dependent on the particular goals, for example, getting a certain latitude coverage at a certain season. Once the star list is finalized, each occultation is designed in detail. When possible, the integration cadence is chosen to achieve a vertical sampling smaller than 5 km. The detector gain is optimized for each star to maximize the signal while avoiding detector saturation. The length of the occultation is chosen to ensure an adequate baseline to establish the unattenuated signal before (for ingress) or after (for egress) the starlight is affected by transmission through the atmosphere.

At the time of writing, 12 stellar occultation campaigns have been executed, on average one campaign every 2 to 3 months. Table 1 lists the date and the corresponding orbit numbers for each occultation campaign including the sequence of the targeted stars. The "Total" column contains the number of all occultations executed during the campaign and the "Used" column occultations that are used in this paper. The "Not Used" column describes the reason that an occultation is not considered in this study. "Altitude Range" means that the occultation was recorded either below the limb of the planet or at altitudes that are outside the range of interest. In the FUV wavelength range, "Stray Light" means that first-order stray light from the MUV channel contaminated the FUV signal at a level that made the analysis difficult. We expect that development of more sophisticated stray light correction algorithms will allow analysis of many of these profiles but here we included only occultations for which stray light can be removed using a simple algorithm, described in the following sections. The third and last column in the "Not Used" section is used for unforeseen events, for example, commanding errors and downlink problems. In total, 780 stellar occultations have been recorded. From these, 406 FUV occultations and 163 MUV occultations have been used to determine density and temperature profiles.

The geographic distribution of stellar occultations is shown in Figures 1a–1c. The latitude distribution in Figure 1a shows a coverage from around 80°S up to around 75°N. The regular longitude sampling discussed above is apparent in this figure. The solar longitude (L_s) of Mars is shown in Figure 1b. IUVS stellar occultation campaigns to date have covered a Martian year (MY). The first stellar occultation campaign was executed during winter in the northern hemisphere (NH) at $L_s = 315°$, and the latest stellar occultation campaign included in this study was performed at $L_s = 298°$. Figure 1c shows the local time coverage.

Journal of Geophysical Research: Planets

10.1029/2017JE005466

Table 1
Overview of the First 12 Stellar Occultation Campaigns

Campaign	Date	Martian year (Sols)	Orbit	L_s	Channel	Total	Used	Not used			Sequence of stars
								Altitude	Stray light	Other	
1	24–26 Mar 2015	32 (585)	00935–00944	314.52°	FUV	60	20	31	9		γ^1 Vel, ϵ CMa, χ Car, κ Vel, τ Sco, λ Sco, λ Sco,
					MUV	60	4	31	24	1	ζ Oph, α Lyr, β Cep, δ Per, β Tau
2	17–18 May 2015	32 (637)	01222–01226	343.82°	FUV	40				40	star, ϵ Ori, β CMa, ϵ CMa, γ^1 Vel, α Vir, α Lyr, β Cep
					MUV	40	25		10	5	
3	1–2 Aug 2015	33 (43)	01635–01640	21.53°	FUV	50	43	4		3	η UMa, γ^1 Vel, ϵCMa, ζ CMa, ϵCMa, γ^1 Vel,
					MUV	50	9	4	35	2	ζ Pup, α Leo, η UMa, α Leo
4	22–23 Sep 2015	33 (93)	01911–01916	45.37°	FUV	55				55	η UMa, α Pav, α Gru, α Eri, γ^1Vel, ζ Pup, ϵ CMa,
					MUV	55				55	α CMa, κ Vel, α Leo, α Pyx
5	3–4 Nov 2015	33 (134)	02132–02137	63.81°	FUV	65	34			31	η UMa, η UMa, σ Sgr, λ Sco, α Pav, κ Sco, α Pav,
					MUV	65	15		25	25	α^1 Cru, γ^1 Vel, ϵ CMa, α CMa, δ Ori, β Tau
6	18–19 Jan 2016	33 (208)	02533–02538	97.00°	FUV	70	30	5	34	1	β Cen, η Aur, α Lyr, β Cep, α Lyr, ζ Oph, δ Sco, τ Sco,
					MUV	70	5	5	55	5	μ^1 Sco, ζ Cen, β Cen, α Mus, δ Sco, η Lup
7	17–18 Mar 2016	33 (265)	02848–02853	124.04°	FUV	50	39	10	1		γ^1 Vel, α Eri, ζ Cas, α Lyr, α Leo, β Cep, β Cep,
					MUV	50	25	10	15		η UMa, η UMa, γ^1 Vel
8	26–27 May 2016	33 (334)	03223–03228	158.96°	FUV	50	40		12		η Cen, γ Lup, α^1 Cru, α Eri, α Gru, γ Peg, α And,
					MUV	50	5		45		γ Peg, α And, γ Cas
9	14–15 Jul 2016	33 (381)	03489–03493	185.98°	FUV	50	45			5	ζ Cen, β Lup, γ^1 Vel, κ Vel, β Cru, β Cen, λ Sco,
					MUV	50	5		40	5	α Pav, σ Sgr, γ Peg
10	21–22 Sep 2016	33 (449)	03856–03865	227.17°	FUV	110	11			99	κ Vel, ζ CMa, δ Cen, α^1 Cru, ζ Cen, β Cen, δ Lup,
					MUV	110				110	β Cen, β Lup, σ Sgr, λ Sco
11	16–18 Nov 2016	33 (503)	04146–04155	263.10°	FUV	100	85	10	5		γ Cas, β CMa, ϵ CMa, γ^1 Vel, ζ CMa, ϵ CMa, κ Vel,
					MUV	100	50	10	40		α^1 Cru, δ Sco, τ Sco
12	11–13 Jan 2017	33 (558)	04436–04446	297.62°	FUV	80	59		20	11	γ Peg, α Eri, α Eri, γ^1 Vel, κ Vel, ζ CMa, γ^1 Vel, η UMa
					MUV	80	20		49	11	
			Total number of FUV occultations			780	black406				
			Total number of MUV occultations			780	black163				

Note. The solar longitude L_s represents the average value during a campaign, and the Martian day number (sols) number is for the begin of the occultation campaign.

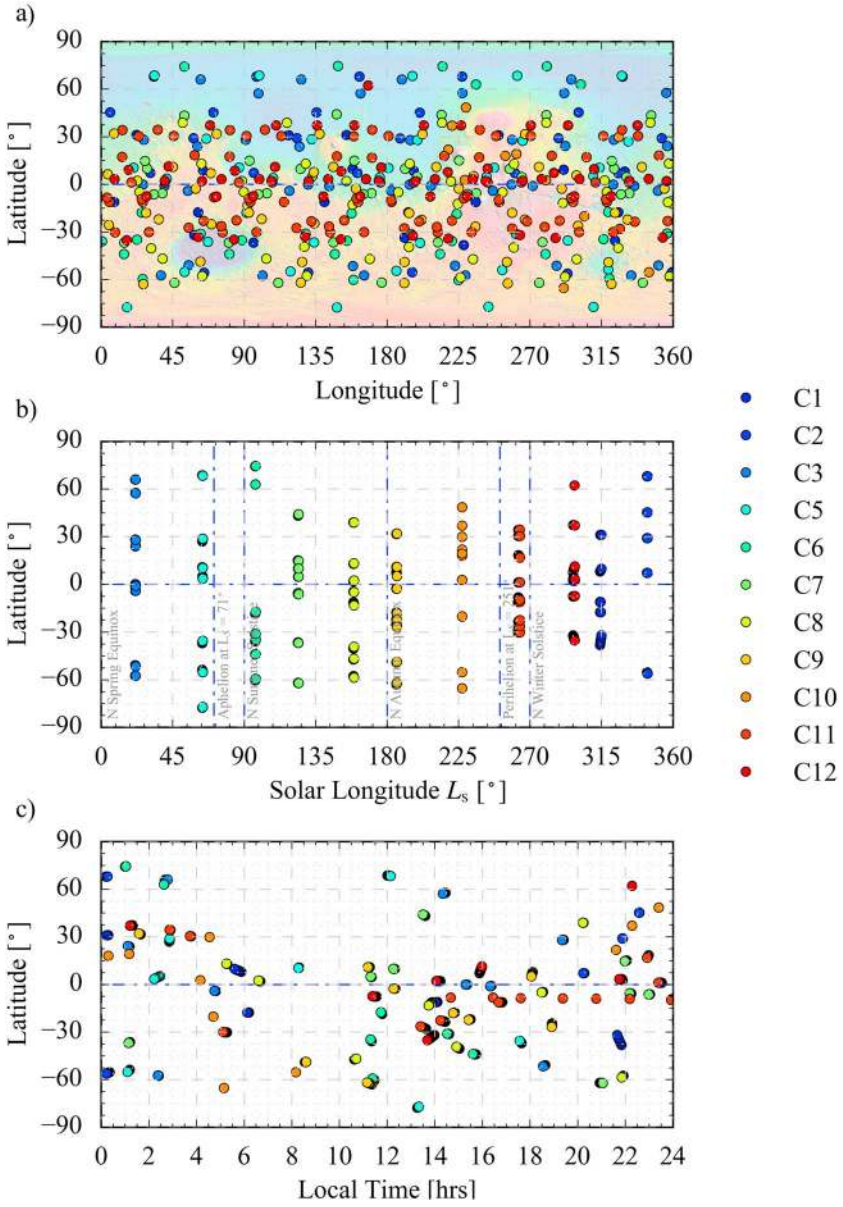

Figure 1. Overview of the geographic coverage of occultations included in this study. (a–c) The distributions with latitude, solar longitude, and local time. Campaigns (C1–C12) are represented by different colors as indicated in the legend. The same color scheme is used in figures throughout the paper when colors refer to campaigns.

3. Data Reduction and Analysis

Reduction of the occultation data to number density and temperature profiles requires calculation of the observing geometry, correction of measurements for dark current, cosmic ray events, atmospheric emissions, and stray light, and division of the attenuated spectra by unattenuated spectra to produce transmission spectra. These are fit with a model for the transmission of the atmosphere to derive LOS column densities that are then inverted to obtain local densities. These steps are described in the following subsections.

3.1. Calculation of the Occultation Geometry

The geometry (altitude, latitude, longitude, local time, solar longitude, and solar zenith angle) for stellar occultations is calculated using SPICE kernels provided by National Aeronautics and Space Administration's Navigation and Ancillary Information Facility. To calculate appropriate altitudes and geometry, the right ascension (RA) and the declination (DEC) of the targeted star have to be adjusted to the actual date of the occultation

according to the proper motion of the star. The values for RA, DEC, and the proper motion are taken from the Hipparcos catalog (Perryman et al., 1997). After loading the SPICE kernels, the position of Mars (target) as seen by MAVEN (observer) in the target frame is calculated. Only a one-way light time aberration correction is used; no additional stellar aberration correction is required, because the absolute position of the stars are known. The two vectors (Mars to MAVEN and Mars to star) define the LOS. The derived geometry is highly accurate because it depends only on the spacecraft trajectory and location of the star, both of which are well known. In particular, errors in spacecraft pointing are not a concern as long as the star appears in the keyhole, which has been the case for all MAVEN occultations. Uncertainties in RA and DEC are less than 1 mas (1 mas = 10^{-3} arcsec $\approx 3\times10^{-7}$°). For the proper motion, the uncertainty is in most of the cases around 5%, still negligible, because the proper motion is only a few tens of milliseconds of arc per year.

The geographic coordinates, altitude, latitude, longitude, and local time for the occultations are defined relative to the lowest-altitude point along the LOS. All coordinates are measured in the planetographic coordinate system with longitude positive eastward. We calculate altitudes above an idealized shape for the Mars surface, modeled as an ellipsoid of revolution with an equatorial radius of 3,396.19 and polar radius of 3,376.20 km.

The spatial distribution of the recorded signal is used to determine the pointing stability. We find that 84% of the occultations have pointing variations of less than 0.021 mrad, 98% have variations less than 0.042 mrad, and 100% have variations less than 0.063 mrad. All these values are small compared with the small keyhole size of 5×7 mrad (less than 1.25%). We expect the stability in the spectral dimension to be similar, implying that spectral shifts during an occultation are not an issue. We therefore assume a constant wavelength shift during an occultation. Spectral fits to the measured transmission spectrum, discussed in section 3.4, are consistent with this assumption.

3.2. Signal Correction

The recorded signals require several corrections before they can be used to measure atmospheric transmission. These include subtraction of dark current, cosmic ray events, atmospheric emissions, and stray light.

3.2.1. Dark Current

The detector dark current is low and subtraction is straightforward. We use observations of dark sky obtained between 7 and 17 s before the occultations to obtain the dark current on each pixel and subtract this from the occultation measurements.

3.2.2. Cosmic Ray Correction

A cosmic ray event is a noticeable spike in the signal that covers a broad wavelength region. Figures 2a and 2b show raw occultation data, corrected only by dark current subtraction, before and after cosmic ray removal. To correct the spectrum for cosmic rays, the light curve L for each spectral and spatial bin is fitted by a function of the form

$$L(r) = \exp\left(-\exp\left(-\sum_n a_n \left(r - r_0\right)^n\right)\right), \quad (1)$$

where r equals the altitude (record) and r_0 and a_n are the exponential coefficients. This correction is needed to determine the altitude where the stellar signal is no longer present. The signal at these altitudes is important for the removal of background due to atmospheric emissions. A cosmic ray event is found when the normalized signal is higher than 0.75% at altitudes where the signal is already completely absorbed. This threshold was retrieved with an empirical approach, finding the right balance between the correction of cosmic ray events but avoiding correction of random noise in the spectrum. The cosmic ray correction is only applied to altitudes where the stellar signal is completely absorbed.

3.2.3. Atmospheric Emission Correction

In addition to the stellar signal, the IUVS occultation data contains nonnegligible signals from atmospheric emissions of H Lyman α at 121.6 nm and OI emissions at 130.4 and 135.6 nm. The main entry ways for this contamination are the keyholes at the end of the IUVS slit. Because the emissions are spatially extended and the keyholes wider than the IUVS slit, the recorded lines are broad and contaminate sizable spectral regions centered on the wavelengths of the spectral lines. Figure 3 shows that the H Lyman α airglow contamination is easily recognized as a trapezoidal shape (black dash-dotted line) underlying the narrower stellar signal.

In order to separate the actual stellar signal and the contamination due to the airglow, we model the spatial distribution of the signal as the sum of a Gaussian profile for the stellar signal and a trapezoidal pedestal for the atmospheric emissions. We use data within 2 standard deviations of the center of the Gaussian profile

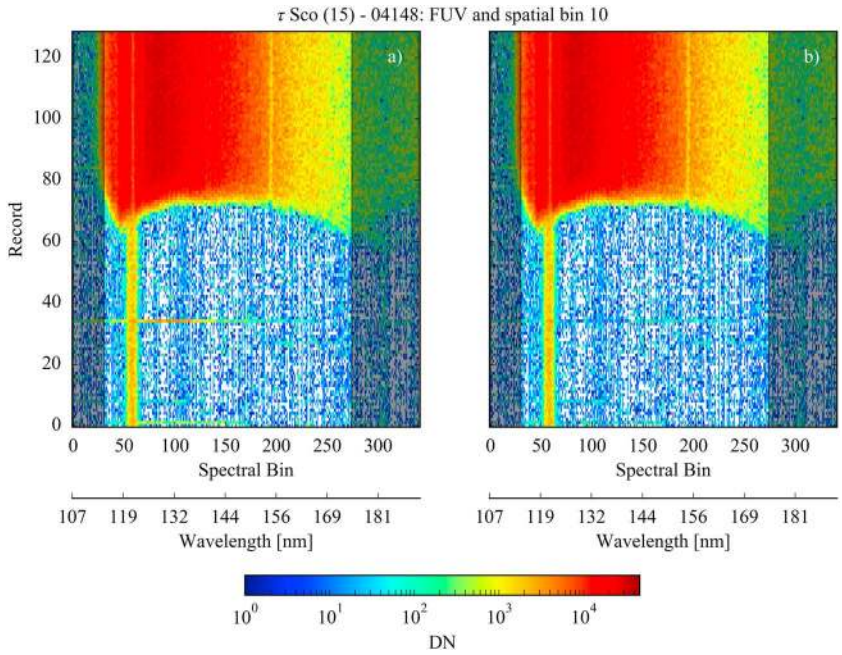

Figure 2. The recorded FUV spectrum of τ Sco executed on 16 November 2016 at 23:50:50 (orbit 04148) for spatial bin 10. (a) The uncorrected spectrum where two cosmic ray events can be seen; one event at record number 35 and a less pronounced event below the limb at record number 1. (b) The cosmic ray corrected version of the spectrum. The gray shaded areas on both sides of each image are not used for the retrieval process. FUV = far ultraviolet.

to extract the stellar signal. The spatial size of the pedestal is correlated with the keyhole and ranges from spatial bins 19 to 36 for the large keyhole and from 5 to 15 for the small keyhole. The atmospheric emissions are present at all altitudes. We assume that they are constant with altitude and calculate a mean value over altitudes where no stellar signal is detected and subtracted this from the signal. Figure 4 shows an example of the original and corrected light curve near H Ly-α. Removal of atmospheric emissions is essentially a downward displacement of the light curve.

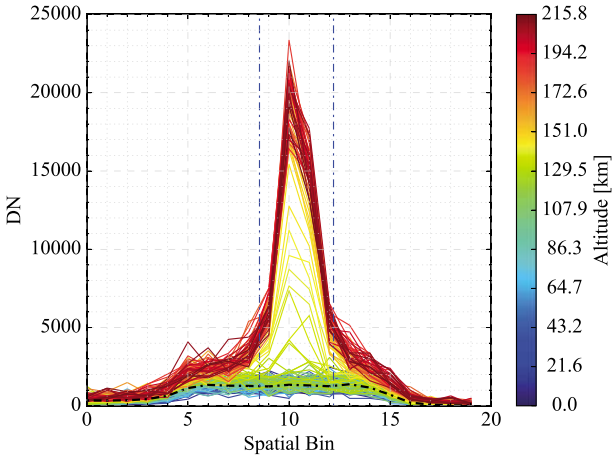

Figure 3. H Lyman α contamination of the signal for λ Sco executed on 26 March 2015 at 11:48:21 (orbit 00943) as a function of detector spatial bin for the spectral bin centered at 121.25 nm. Altitude is coded by color with blue colors represent lower altitudes and red colors higher altitudes. The vertical blue dash-dotted lines indicate the 2σ standard deviation of the central, Gaussian-like peak. Our model for the contribution of atmospheric emission to the signal is illustrated by the black dash-dotted line.

3.2.4. Stray Light Correction

Observations made of the dayside or near the relatively bright terminator are often contaminated with stray light with a spectral shape consistent with the solar spectrum scattered from Mars. This stray light is a serious problem for dayside MUV occultations. It also plagues FUV occultations through first-order MUV emissions, which show up in the FUV, albeit at a greatly reduced level. In fact, this stray sunlight usually only causes problems in the FUV channel if the MUV detector is saturated by stray light, because this prevents us from using the MUV signal to correct the FUV signal. Algorithms to remove the stray light contamination are under development. For the data analyzed here, we correct a small number of FUV occultations for which the stray light appears only in the altitude regions where the FUV starlight is fully attenuated. This allows us to examine many dayside occultation measurements.

3.3. Calculation of the Transmission Spectrum

In order to analyze atmospheric absorption, we define a transmission spectrum $T_{i,j}$ for the jth spectral bin and the ith LOS as

$$T_{i,j} = S(z_i, \lambda_j)/S_0(\lambda_j), \tag{2}$$

the ratio of the attenuated spectrum, $S(z_i, \lambda_j)$, to a reference spectrum, $S_0(\lambda_j)$, obtained as the average spectrum at altitudes where attenuation is negligible. For a typical occultation, absorption signatures are present up to ~160 km; therefore, we use the regions above 180 km to define

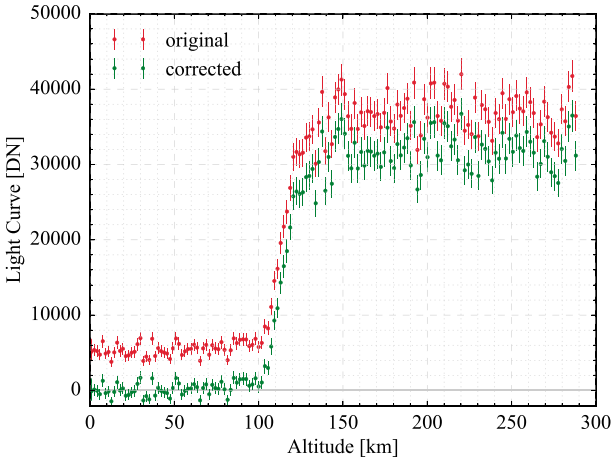

Figure 4. Measured and atmospheric emission corrected light curve for λ Sco executed on 24 March 2015 at 23:43:54 (orbit 00935) in red and green, respectively, for a wavelength of 121.57 nm.

the reference spectrum. A single stellar occultation takes between 3 and 13 min, with a mean duration of 5:30 min, and thus, attenuated and reference spectra are recorded nearly at the same time and changes stellar output or instrument response due to temperature variation, sensitivity drift, etc., are negligible.

We adopt an empirical approach to determine the errors in the transmission spectrum. We measure the time variation of the signal in the unattenuated region of the occultations assuming that these variations represent random measurement errors. We further assume that the errors are independent of wavelength. This allows us to determine the dependence of random uncertainty on signal strength. Figure 5 shows the standard deviation divided by the mean versus the signal. Errors are calculated individually for each occultation using this technique.

3.4. Fitting the Transmission Spectrum

The next step in the analysis is to fit the transmission to determine the LOS column abundances for the absorbing species. The absorption of the stellar irradiance $F_0(\lambda)$ by the atmosphere along the LOS, between the star and the IUVS instrument, can be described via the Beer-Lambert law:

$$F(\lambda, z) = F_0(\lambda)e^{-\tau(\lambda,z)} \tag{3}$$

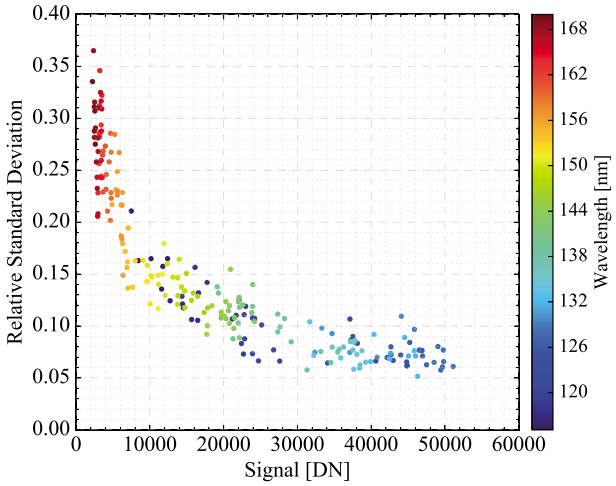

Figure 5. Relative standard deviation (standard deviation divided by the mean) depending on the signal for η Cen executed on 26 May 2016 at 14:56:54 (orbit 03223). Each data point represents a single spectral bin of the detector.

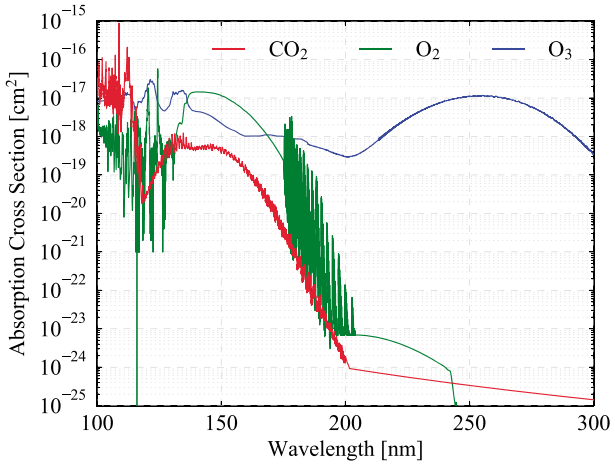

Figure 6. CO_2, O_2, and O_3 absorption cross sections used for the spectral inversion.

with τ the optical depth, related to LOS column abundances by

$$\tau(\lambda, z) = \Sigma_k \sigma_k(\lambda) N_k(z) + \tau_{\lambda_0} \left(\frac{\lambda_0}{\lambda} \right)^{\alpha}, \tag{4}$$

where N_k is the LOS column density of the kth species and σ_k its absorption cross section, assumed constant along the LOS. Based on previous results and visual examination of the spectra, we consider only absorption due to CO_2, O_2, and O_3. The last term in equation (4) represents extinction by aerosols, which is modeled by a simple power law dependence on wavelength. The exponent α is referred to as the Angström coefficient (Dubovik et al., 2000; Montmessin et al., 2006). Absorption by CO_2, O_2, and O_3 shows distinctive absorption features (cf. Figure 6), but extinction due to aerosols is smooth and affects the whole wavelength range.

LOS column abundances for each tangent altitude are determined by fitting the measured data with a model for the transmission spectrum using the Levenberg-Marquardt algorithm. The model transmission for the jth LOS in wavelength bin λ_i is calculated through

$$\mathcal{T}_{i,j} = \frac{\int \mathrm{d}\lambda' \, R(\lambda', \lambda_i) F(\lambda', z_j)}{\int \mathrm{d}\lambda' \, R(\lambda', \lambda_i) F_0(\lambda')}, \tag{5}$$

where $R(\lambda', \lambda_i)$ is the instrument line spread function. The integrals in equation (5) are carried out at a resolution of 0.08 nm to accurately account for the high-resolution structure in the absorption cross sections and solar spectrum.

The uncertainties of the fitted parameters are obtained directly from the Levenberg-Marquardt algorithm as the square root of the diagonal terms of the returned covariance matrix. A Monte Carlo approach was used to check this procedure. We generated 500 synthetic transmission spectra, varying around the original transmission spectrum assuming a Gaussian distribution of errors with a standard deviation determined from Figure 5. Each synthetic transmission spectrum is fit in the same manner as the original data, resulting in a distribution of the fitted parameters. The standard deviation of this distribution provides an estimate of the uncertainty in the fit parameters, and it is in agreement with the uncertainties delivered by the Levenberg-Marquardt algorithm. We use the latter because the Monte Carlo approach is computationally burdensome.

We analyze the FUV and MUV transmission simultaneously because CO_2 absorption is seen in both channels. We have found that the optimal way to combine the two regions is to use the FUV spectrum up to 175 nm and the MUV spectrum for wavelength longer than 175 nm. This means ignoring the FUV signal between 175 and 190 nm. We determined empirically that inclusion of these data did not improve results, likely because of the low signal-to-noise ratio (SNR) in this region of the FUV channel.

Absorption cross sections for the spectral inversion are needed to fit the CO_2, O_2, and O_3 abundances. We assumed a mean temperature in the Martian atmosphere of 180 K, and the absorption cross sections closest to the available temperature are used. The cross sections are shown in Figure 6. The CO_2 absorption dominates the spectrum at wavelengths shortward of 200 nm, but small and distinctive O_2 features can be seen

Table 2
Photoabsorption Cross Sections

Wavelength range (nm)	Temperature (K)	Reference
	CO_2	
89.03930–109.89010	195	Archer et al. (2013) and Stark et al. (2007)
109.89560–118.70130	195	Stark et al. (2007)
118.70390–163.37020	195	Yoshino et al. (1996)
163.37300–192.48810	195	Parkinson et al. (2003)
192.48970–199.98835	295	Parkinson et al. (2003)[a]
200.00000–201.58000	298	Ityaksov et al. (2008)[b]
200.00000–320.00000	—	Huestis and Berkowitz (2011)
	O_2	
100.00000–107.70000	298	Matsunaga and Watanabe (1967)
107.97441–108.70008	295	Wu et al. (2005)
108.75000–114.95000	298	Ogawa and Ogawa (1975)
115.00000–132.00000	303	Lu et al. (2010)
132.04000–175.24000	295	Yoshino et al. (2005)
175.43860–204.07954	130–500	Minschwaner et al. (1992)
194.00000–240.00000	298	Yoshino et al. (1988, equation 3)
240.88843–244.99820	287–289	Fally et al. (2000)
245.00000–320.00000	—	set to zero (above the dissociation limit)
	O_3	
99.0000–108.5000	295	Ogawa and Cook (1958)
110.1510–184.6484	295	Mason et al. (1996)
184.9223–213.3341	195	Yoshino et al. (1993)
213.3400–320.0000	193	Serdyuchenko et al. (2014)

[a]Shifted by a factor of 0.45 to adopt for the different temperature. [b]Used the Rayleigh scattering corrected cross sections and shifted by a factor of 0.45 to adopt for the different temperature.

at 120.6 and 124.6 nm and O_2 absoprtion in the Schumann-Runge continuum alters the slope of the spectrum in the 140- to 160-nm region. Ozone shows a distinctive feature in the Hartley bands, a broad absorption feature centered around 255 nm. Thus, O_2 absorption is detected in the FUV channel, O_3 in the MUV channel, and CO_2 in both.

Several sources have been combined to get the CO_2 absorption cross section over the wavelength range from 100 to 300 nm. Rayleigh scattering by CO_2 is included for wavelengths longer than 202 nm. A composite absorption cross section for O_2 is used again to cover the wavelength range. When available we used cross sections measured at a temperature of 195 K. The O_3 absorption cross section shows no temperature dependence in the wavelength range of interest. Table 2 shows the sources for the cross sections along with the wavelength range and temperature range of the measurements. A detailed description of the temperature sensitivity of the retrieval process can be found in Sandel et al. (2015).

Figure 7 shows a sample of a measured transmission spectrum for the combined FUV and MUV channels at two different altitudes and the corresponding best fit transmission. The separate contribution of CO_2, O_2, and O_3 and aerosols is also shown. Shaded areas represent the uncertainties obtained from the fitting algorithm. In panel (a), at an altitude of around 30 km, the O_2 column density is tied to 2×10^{-3} of the CO_2 column density. In panel (b), at around 110 km, no contribution due to aerosols and ozone can be seen and their transmission is unity. At 30 km, significant absorption can be seen around 250 nm due to ozone. Furthermore, a decrease of the transmission spectrum over the whole wavelength range due to the aerosols (orange line) can be noticed. In this example around 30% of the stellar signal gets absorbed by aerosols. In contrast, the transmission at 110 km shows no absorption due to ozone and aerosols. The main contribution to the absorption in the FUV

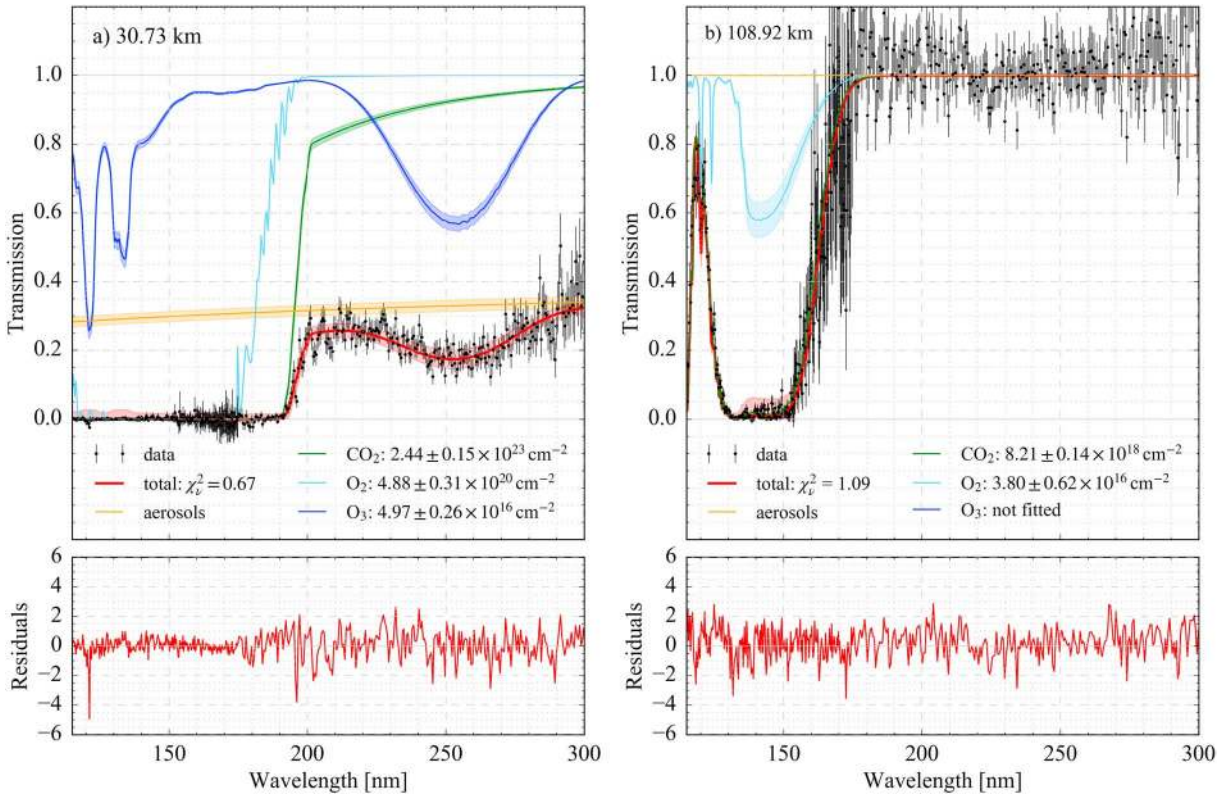

Figure 7. Transmission spectrum of the combined far ultraviolet and mid-ultraviolet channels for γ ^{1}Vel executed on 17 March 2016 at 12:40:25 (orbit 02848) and two different altitudes at around 30 and 110 km, panels (a) and (b), respectively; measurements including their uncertainties in black and the best fit in red with the reduced chi-square χ^2_ν. The contribution of CO_2, O_2, and O_3 including their fitted column densities and from the aerosol to the fitted transmission spectrum are shown in green, light blue, blue, and orange, respectively. Shaded areas covering the fitted transmission spectra represent the uncertainties obtained from the fitting algorithm. The lower panels show the residuals between the measured and the modeled transmission spectra. The residual is calculated as the difference between the measured and the fitted transmission divided by the measured transmission uncertainty.

wavelength range is due to CO_2 and O_2. As one can see, the absorption in the Schumann-Runge continuum of O_2 affects the slope near 150 nm. Moreover, two sharp O_2 bands at 120.6 and 124.6 nm produce distinctive features that can be seen on the low wavelength side of the CO_2 absorption band.

We obtain best results by fitting the spectra in three steps: determine (1) the wavelength shift, (2) the O_2 abundance, and (3) the CO_2 and O_3 abundances together with the aerosol optical depth and the Angström coefficient. We determine the wavelength shift using only the FUV channel as it has sharper spectral features than the MUV. This is permissible because the FUV and MUV spectral shifts are affected in the same way by spacecraft pointing. We fit the tranmission spectrum at each altitude with the CO_2 and O_2 column densities and the wavelength shift as free parameters. The initial guess for the wavelength shift is determined empirically from comparison of the data to synthetic transmission spectra, relying on the distinctive absorption features in the molecular cross sections. Fits are applied only where CO_2 is not saturated ($> \approx$100 km). As shown in Figure 8, the derived wavelength shifts for low SNR occultations display point-to-point variations, which must be noise rather than oscillations of the spacecraft. For occultations with high SNR the wavelength shifts derived from these fits are much more constant with altitude than for occultations with lower SNR (Figure 8). We therefore assume that the wavelength shift is constant with altitude within an occultation and set it equal to the mean value of the fit results. This wavelength shift is held constant in subsequent steps.

Next, we consider the O_2 distribution in the atmosphere. O_2 is only detectable in the FUV spectral region and at high altitudes, typically above ~90 km. In this step, we keep the CO_2 and O_2 column densities as free parameters but fix the wavelength shift to the constant value that was obtained in the first step. The O_2 column densities determined in the fits appear reasonable but are sometimes noisy, and moreover, the O_2 noise can induce noise in the retrieved CO_2 column density. Physically, we expect the O_2/CO_2 ratio to vary smoothly with altitude. We therefore fit the ratio of O_2 to CO_2 column abundance with a power law and replace the O_2 column

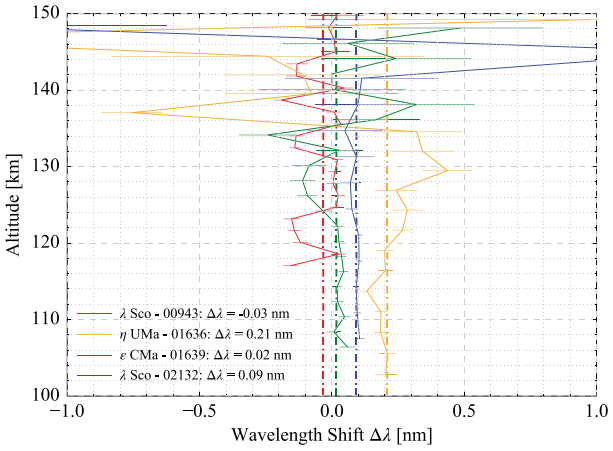

Figure 8. Spectral shifts for four different occultations. The solid lines show the actual fitted value including the uncertainties. The dash-dotted lines indicate the constant wavelength shift used in the analysis.

density with the fit (Figure 9). The fit is extended downward until the ratio of O_2 to CO_2 column densities reaches a value of 2×10^{-3}, below which the ratio is set equal to this value. As shown in Figure 9, the power law provides an excellent fit to the observations. The increase in the O_2/CO_2 ratio with altitude is expected because O_2 is created by photochemistry at high altitudes and is lighter than CO_2 and therefore enhanced at high altitude by diffusive separation, but here we simply treat the O_2 mixing ratio model as an empirical fit to the data. The asymptotic ratio of 2×10^{-3} is consistent with the bulk of the occultation results but is not necessarily correct for any individual occultation. This has little affect on our results because the occultation is no longer sensitive to O_2 density as long as it is of order 10^{-3}. The procedure described above works for O-type stars and B-type stars down to the subclass B3. However, for cooler stars, B-type stars with a subclass number higher than B3 and A-type stars, the retrieval of the O_2 is not included because stellar emission is too weak in the wavelength region containing the distinctive O_2 features. Therefore, for IUVS stellar occultations targeting α Gru (B7), α Lyr (A0), β Tau (B7), α Leo (B7), and α And (B8) we simply confine the wavelengths analyzed to longer than 126 nm and fix the O_2/CO_2 column density ratio at 2×10^{-3} and fit for only CO_2, O_3, and aerosols.

The third and final fit is performed with the constant wavelength shift and the smooth O_2 profile determined in the earlier steps. This fit determines the CO_2 and O_3 column density profiles, the aerosol optical depth at a reference wavelength of 250 nm, and the Angström coefficient. The full set of results for an occultation of γ ^{1}Vel is shown in Figure 9.

3.5. Vertical Inversion

Local number densities are obtained from the LOS column densities by a vertical inversion. Our approach is based closely on that described in Quémerais et al. (2006), but we have made a number of significant improvements and therefore present a complete description of the algorithm currently in use.

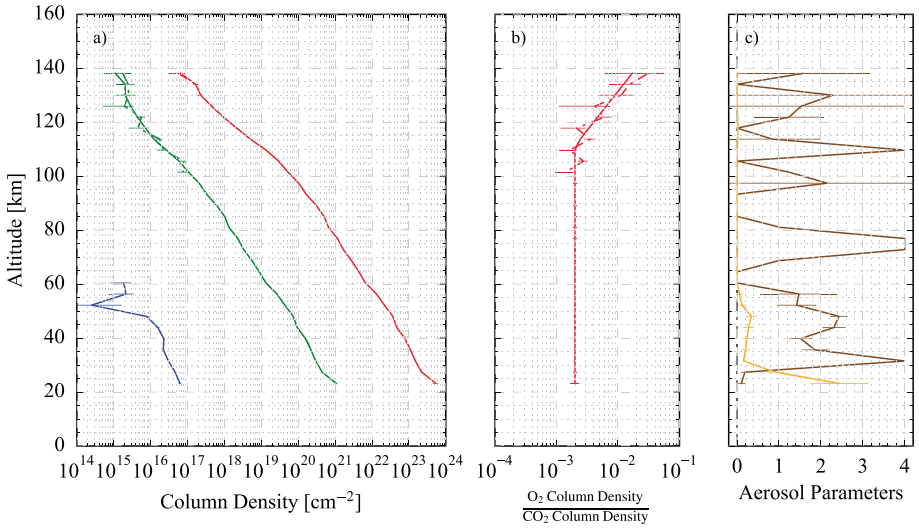

Figure 9. Results of spectral fits to the γ ^{1}Vel occultation executed on 17 March 2016 at 12:40:25 (orbit 02848). (a) The retrieved column densities for CO_2 (red), O_2 (green), and O_3 (blue). The dash-dotted lines indicate the original fit (O_2 column density free to vary), whereas the solid lines show results with the with a fixed value for the ratio of O_2 to CO_2 column density. (b) The dash-dotted line shows the O_2/CO_2 column density ratio from the spectra fits, and the solid line shows the smoothed profile used in the fits of CO_2, O_3, and aerosols. (c) The retrieved aerosol optical depth τ at 250 nm and the Angström coefficient α are shown in orange and brown, respectively.

The LOS column density N_j is the integral over the local number density n along the LOS. Assuming spherical symmetry, we have

$$N_j = 2\int_{a_j}^{+\infty} n(r)\frac{r}{\sqrt{r^2 - a_j^2}}\mathrm{d}r \tag{6}$$

with a_j as the radius distance of the lowest point along the LOS to the center of Mars, r the radius distance to a point in the atmosphere, and $n(r)$ as the local number density at that point. Dividing the atmosphere into discrete layers, this expression can be written in matrix notation as

$$\mathbf{N} = \mathbf{K}\cdot\mathbf{n}, \tag{7}$$

where **N** represents the vector containing the N_j values and **n** the vector of the local number densities at the center of the layers. The **K** matrix represents the LOS integration:

$$K_{ji} = 2\int_{r_i-1/2}^{r_{i+1/2}} f(r)\frac{r}{\sqrt{r^2 - a_j^2}}\mathrm{d}r, \tag{8}$$

where i indicates the atmospheric layer and j the LOS. The function $f(r)$ gives the variation of the local number density in the layer. We assume that $f(r) = 1$, which is accurate for sufficiently thin layers.

According to equation (8) in Quémerais et al. (2006) an estimator for the local number density $\mathbf{n_0}$ can be obtained by

$$\mathbf{n_0} = \mathbf{S}_{\mathbf{n_0}}\mathbf{K}^{\mathsf{T}}\mathbf{S}_{\mathrm{e}}{}^{-1}\mathbf{N}, \tag{9}$$

where $\mathbf{S}_{\mathbf{n_0}}$ is the covariance matrix associated with this estimator given by

$$\mathbf{S}_{\mathbf{n_0}} = \left(\mathbf{K}^{\mathsf{T}}\mathbf{S}_{\mathrm{e}}{}^{-1}\mathbf{K}\right)^{-1}. \tag{10}$$

$\mathbf{S}_{\mathrm{e}}$ is a diagonal matrix with elements equal to the square of the standard deviation σ_i associated with the slant column density N_i obtained from the spectral inversion:

$$\left(\mathbf{S_e}\right)_{ij} = \sigma_i^2\delta_{ij}. \tag{11}$$

The uncertainties $\mathbf{ffin_0}$ of the retrieved number densities $\mathbf{n_0}$ are calculated from $\mathbf{S}_{\mathbf{n_0}}$ via

$$(\delta \mathrm{n}_0)_i = \sqrt{\left(S_{\mathrm{n}_0}\right)_{ii}}. \tag{12}$$

In most cases, the solution described above causes an amplification of the noise. Quémerais et al. (2006) used the Tikhonov regularization method (Tikhonov & Arsenin, 1977; Twomey, 1977) to lessen this effect. This is done by including a smoothness constraint to the inversion:

$$\mathbf{n} = \mathbf{S}_{\mathrm{n}}\mathbf{K}^{\mathsf{T}}\mathbf{S}_{\mathrm{e}}{}^{-1}\mathbf{N}, \tag{13}$$

where $\mathbf{S}_{\mathrm{n}}$ is given by

$$\mathbf{S}_{\mathrm{n}} = \left(\mathbf{K}^{\mathsf{T}}\mathbf{S}_{\mathrm{e}}{}^{-1}\mathbf{K} + \mathbf{L}^{\mathsf{T}}\mathbf{S}_{\mathrm{s}}{}^{-1}\mathbf{L}\right)^{-1} \tag{14}$$

with $\mathbf{S}_{\mathrm{s}}$ defined by

$$\mathbf{S}_{\mathrm{s}}{}^{-1} = \lambda_{\mathrm{s}}\mathbf{I} = \begin{pmatrix} \lambda_{s_1} & 0 & 0 & \cdots & 0 & 0 & 0 \\ 0 & \lambda_{s_2} & 0 & \cdots & 0 & 0 & 0 \\ 0 & 0 & \lambda_{s_3} & \cdots & 0 & 0 & 0 \\ \vdots & \vdots & \vdots & \ddots & \vdots & \vdots & \vdots \\ 0 & 0 & 0 & \cdots & 0 & \lambda_{s_{k-1}} & 0 \\ 0 & 0 & 0 & \cdots & 0 & 0 & \lambda_{s_k} \end{pmatrix}, \tag{15}$$

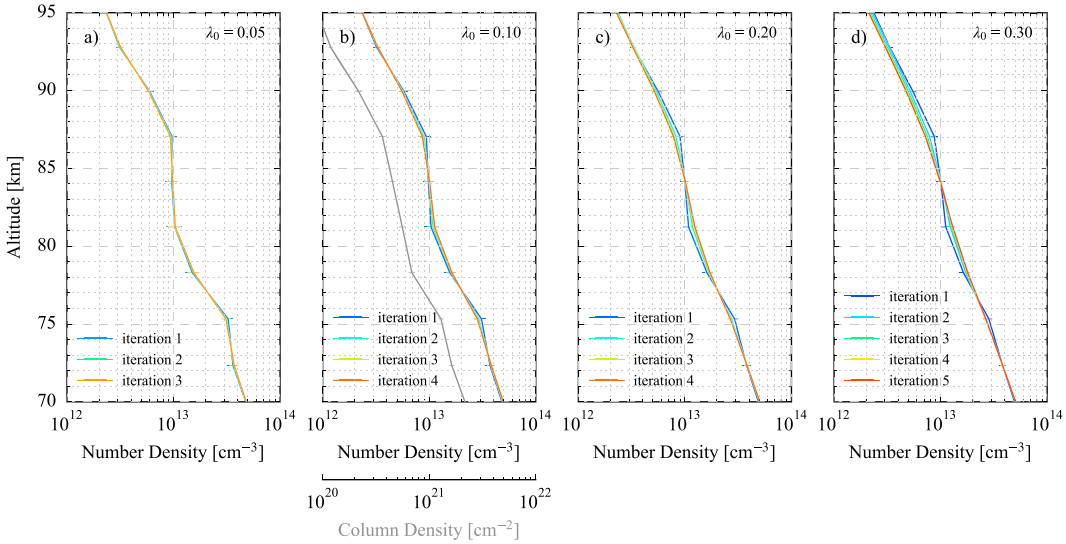

Figure 10. (a–d) Number density profiles for η UMa executed on 1 August 2015 at 15:09:17 (orbit 01635) using different smoothing coefficients λ_0 = 0.05, 0.10, 0.20, and 0.30 for the Tikhonov regularization. The gray line in panel (b) represents the column number density.

and **L** defined by

$$\mathbf{L} = \begin{pmatrix} -1 & 1 & 0 & 0 & \cdots & 0 & 0 & 0 & 0 \\ 1 & -2 & 1 & 0 & \cdots & 0 & 0 & 0 & 0 \\ 0 & 1 & -2 & 0 & \cdots & 0 & 0 & 0 & 0 \\ \vdots & \vdots & \vdots & \vdots & \ddots & \vdots & \vdots & \vdots & \vdots \\ 0 & 0 & 0 & 0 & \cdots & 0 & 1 & -2 & 1 \\ 0 & 0 & 0 & 0 & \cdots & 0 & 0 & 1 & -1 \end{pmatrix}. \tag{16}$$

L represents a discrete second derivative operator in the interior of the domain and a first derivative operator on the boundaries. In our case, this operator is not divided by the squared distance between two consecutive layers as mentioned in Quémerais et al. (2006), because this effect is incorporated in the smoothing parameter λ_0, discussed below.

The right choice for the smoothing coefficient is a compromise between two aspects, the smoothness and the altitude resolution. Using a low smoothing coefficient gives a poor regularization and results in a noisy number density profile but with an good altitude resolution. Alternatively, choosing a high smoothing coefficient gives a smooth profile but decreases the altitude resolution. Quémerais et al. (2006) obtained good results when the smoothing constraint varies with altitude according to

$$\lambda_{si}(r) = \lambda_0 \frac{1}{\delta n_i^2}, \tag{17}$$

with the single smoothing coefficient λ_0, adjustable to balance smoothness and altitude resolution. We adopt this approach here. Figure 10 shows the effect of different values of λ_0 on **n**. We discuss further the consequences of different choices of λ_0 in the next section.

With this approach, it is necessary to solve for the number densities iteratively because the smoothing coefficients used to derive the number densities also depend upon the number densities, through their uncertainties. The first iteration is without any smoothing to get an estimator for the local number densities and their uncertainties using equations (9) and (10). In the following iterations the Tikhonov regularization, equations (13) and (14), are used and the new errors for the next iteration are calculated. Iterations are continued until convergence satisfies a specified tolerance:

$$\max\left(\left|\frac{{}^{k+1}n_i - {}^{k}n_i)}{{}^{k}n_i}\right|\right) \leq \epsilon, \tag{18}$$

where the index k indicates the iteration number. A tolerance of $\epsilon = 0.01$ is used for the results reported here.

In section 4.5 we interpret wave-like perturbations of the CO_2 number density profile as tides in the thermosphere. This interpretation rests on the conclusion that the observed perturbations are a property of the atmosphere rather than an instrumental or data reduction artifact. We present the arguments in support of this assertion in this section.

Tikhonov regularization represents a smoothing of retrieved densities, and therefore, there is a danger that noise in the data will be spread over several data points by the regularization process and will thus appear as a real feature when it is simply an artifact created by noise combined with smoothing. To demonstrate that this is not the case for the perturbations seen in the densities retrieved from the occultations, we show in Figure 10 both the column density and the local density from a typical occultation. It is clearly seen in Figures 10a and 10b that the wave-like perturbations are present in the column densities, and furthermore, the perturbation amplitudes are not amplified in the inversion process.

On the other hand, we must also be careful that the smoothing in inversion process does not damp or remove real perturbations. To investigate this, we have looked at results obtained with several values of the smoothing coefficient. Figure 10 shows local densities obtained with smoothing coefficients of $\lambda_0 = 0.05$, 0.10, 0.20, and 0.30. With $\lambda_0 = 0.20$ and 0.30 the wave feature seen in the local density are smoothed out, albeit only slightly, implying that some information on wave structures has been lost. With a smoothing coefficient of $\lambda_0 = 0.10$ and 0.05, the wave structures are preserved. Using values lower than 0.10 in the iteration does not lead to substantially different density profiles. Thus, a smoothing coefficient $\lambda_0 = 0.10$ is used for all results presented in this study with an altitude sampling less than 6 km. However, for an altitude spacing higher than 6 km a λ_0 value of 0.01 is used.

We have investigated several other possible sources of artifacts in the local density profiles. For example, when developing our data reduction algorithm, we noticed that noise in the derived wavelength shifts and O_2 densities cause perturbations in the CO_2 densities. The procedures described in the previous sections to treat wavelength shifts and O_2 densities were designed in part to remove these artifacts. Another possible artifact could result from periodic variations in spacecraft pointing that might then appear as a wave in the retrieved column densities. To investigate this, we have compared both wavelength shifts and spacecraft pointing information with the observed perturbations and have not found any correlation (see Figure 8). Thus, we conclude that wave-like perturbations in the derived local densities represent a real characteristic of the Mars atmosphere.

3.6. Calculation of the Temperature

As the dominant constituent in the atmosphere, the CO_2 distribution is in hydrostatic equilibrium and analysis of the density profile can be used to determine the atmospheric temperature. The technique used here to derive temperature profiles follows that described by Snowden et al. (2013). The partial CO_2 pressure at an altitude r_i is calculated by integrating the hydrostatic equilibrium from the upper boundary r_0 down to r_i as

$$P(r_i) = P(r_0) + m_{CO_2} \int_{r_i}^{r_0} n_{CO_2}(r) g(r) \mathrm{d}r, \tag{19}$$

where $n_{CO_2}(r)$ is the smoothed CO_2 number density, $g(r)$ the acceleration of gravity, m_{CO_2} the molecular mass of CO_2, and $P(r_0)$ the pressure at r_0, the upper boundary. The temperature $T(r)$ is calculated from the ideal gas law:

$$T(r) = \frac{P(r)}{k_B n_{CO_2}(r)}, \tag{20}$$

with k_B Boltzmann's constant. The CO_2 number density used in equation (19) has been smoothed using a modified Savitsky-Golay filter with a five-point sliding window in order to damp small scale fluctuations (Snowden et al., 2013).

The pressure at the upper boundary $P(r_0)$ is determined by fitting the measured density above r_0 to the expression for a hydrostatic variation with a constant temperature gradient (Snowden et al., 2013). Typically, we set the upper boundary of the temperature calculations at the altitude for a transmission of 0.95 at 150 nm although for bright stars we find that we can extend the analysis to the altitude where the transmission is 0.98. $P(r_0)$ is determined from the four data points above the upper boundary. Because the temperature gradient

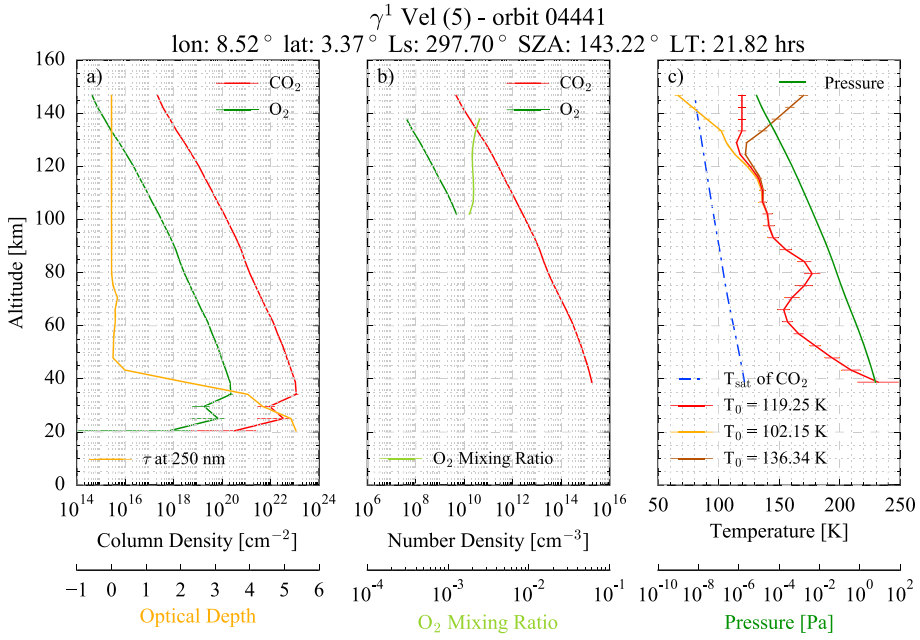

Figure 11. Results obtained during the whole retrieval process for γ ^{1}Vel executed on 12 January 2017 at 05:32:50 (orbit 04441): fitted column densities and the optical depth τ at 250 nm (panel a), inverted number densities and the O_2 mixing ratio (panel b), and the temperature and pressure profiles (panel c). The temperature profiles in orange, red, and brown represent the different upper boundary temperatures T_0. The blue dash-dotted line in panel (c) indicates the CO_2 saturation temperature.

in this region is unknown, we consider values of zero gradient (isothermal) and plus-minus half the adiabatic lapse rate to estimate the uncertainty due to the upper boundary condition.

A Monte Carlo approach is used to determine the uncertainties in the temperature profiles caused by uncertainties in the number densities. We generate 1,000 synthetic density profiles consisting of random densities chosen as elements of a normal distribution with the measured density and its uncertainty defining the mean and standard deviation of the distribution. For each of the synthetic density profiles the corresponding temperature profile is calculated resulting in a distribution of the temperature at each altitude. The temperature uncertainty is set equal to the standard deviation of this distribution.

Figure 11 shows an example of results obtained during the retrieval process from the column densities and the aerosol optical depth τ (panel a), to the local number densities and the O_2 mixing ratio (panel b), to the temperature and pressure profiles (panel c). The temperature profiles show the effects of the different upper boundary temperatures discussed above.

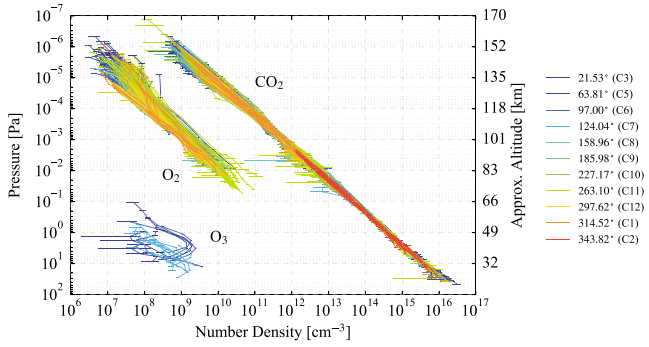

Figure 12. Retrieved CO_2, O_3, and O_2 number density profiles for stellar occultations taken with the Imaging UltraViolet Spectrograph instrument during the first 12 stellar occultation campaigns. Colors represent different solar longitudes L_s as indicated in the legend. The corresponding campaign number is given in parentheses.

4. Results and Discussions

In the previous sections we described the execution of stellar occultations with the MAVEN/IUVS instrument and explained the steps necessary to retrieve number densities and temperature profiles from the measurements. In this section, we provide some initial results. We focus on CO_2, O_3, and O_2 number densities, temperature profiles, and perturbations seen in the CO_2 altitude profiles. We do not discuss aerosol and dust profiles in detail in this paper. The data used in this section are archived in the Planetary Atmospheres Node of the Planetary Data System; we used version 13. We compare our measurements with values determined from previous observations as well as with predicted profiles from the Mars Climate Database (MCD) v5.2. The MCD is derived from the Laboratoire de Météorologie Dynamique Mars Global Climate Model (LMD-MGCM, Forget et al., 1999) extended in the upper atmosphere as described

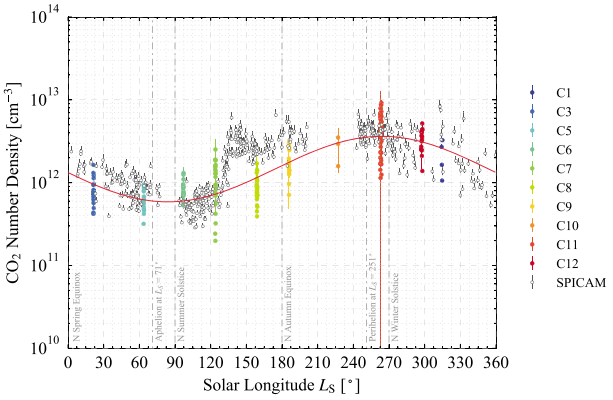

Figure 13. Solar longitude dependence of the CO_2 number density at 100 km. Colors represent the number densities for a different stellar occultation campaign (listed in Table 1). The solid red line shows the sinusoidal least squares fit to the measured densities. In addition, the CO_2 number densities from Mars Express/SPICAM stellar occultations shown in Forget et al. (2009) are included as gray open circles. The Imaging UltraViolet Spectrograph and SPICAM data shown here include measurements at latitudes below 50° and all available longitudes and local times. SPICAM = Spectroscopy for Investigation of Characteristics of the Atmosphere of Mars.

in González-Galindo et al. (2009, 2015) and includes a photochemical model able to simulate the O_3 cycle (Lefèvre et al., 2004, 2008). The MCD contains model output averaged over a Mars month (intervals of 30° of Ls, typically 50–60 sols) at 12 local times. The MCD output covers the entire atmosphere of Mars from the surface to ~250 km with an altitude resolution that ranges from 4 km in the lower atmospheres to 8 km in the upper atmosphere. A horizontal 64 × 49 grid is used for the longitude and latitude resolution in the MCD, resulting in a 5.625° sampling in the longitude and a 3.75° sampling in the latitudinal direction. An overview of the MCD version 5 used here can be found in Millour et al. (2014). The MY covered by MAVEN/IUVS stellar occultations is not yet included in the MCD database; thus, we used the available MY that has an $F_{10.7}$ index (solar radio flux at 10.7 cm at 1 AU) that is closest to that at the time of the occultations; MY26 for campaign 1 and 2, MY27 for campaigns 3–7, and MY28 for campaigns 8–10. Although MY28 was closer to the $F_{10.7}$, index for campaigns 11 and 12, we used MCD MY29 output for these campaigns, as they occurred at times of year with a major global dust storm in MY28.

4.1. CO_2 Density

A survey of the CO_2 density in the upper mesosphere/lower thermosphere of Mars is a main goal of the analysis conducted here. As the main atmospheric component, its density and temperature are key parameters to understand the processes at play in the region of the atmosphere where a number of characteristic processes interact (radiative cooling, dynamics, molecular decomposition, etc.) and where couplings between the lower and the upper atmosphere can be identified. In particular, the role of gravity wave propagation and dissipation and the associated deposition of momentum are still only tentatively understood. Their impact on the mean upper atmospheric circulation remains to be demonstrated by observations, one objective that guides the analysis presented in this investigation. In addition, improving our knowledge of CO_2 density/temperature and its seasonal/spatial variability in the altitude range covered by IUVS will provide engineers with the information needed to prepare the future of Mars' exploration (aerobraking, Entry/Descent/Landing phases).

Figure 12 shows the CO_2, O_3, and O_2 number density profiles as a function of pressure. It is convenient to use the pressure scale to compare the retrieved number densities, as it compensates for temperature differences at lower altitudes. The variation in density at a constant pressure is up to a factor of 3 for CO_2. Because the atmosphere is an ideal gas, the variability in density at constant pressure is due to variability in the local temperature. The variation in O_3 and O_2 is much larger, up to an order of magnitude at some pressures for O_2 and even higher for O_3.

Figure 13 shows the variation of CO_2 number density with L_s at an altitude of 100 km along with the CO_2 number densities derived from SPICAM occultations (Forget et al., 2009). The variation with L_s is similar for the IUVS and SPICAM results but the densities reported here have a higher variability at a given L_s. Although the occultations from the IUVS and the SPICAM instrument are 10 years apart, solar activity as measured by the $F_{10.7}$ index (solar radio flux at 10.7 cm) are comparable. Furthermore, the National Oceanic and Atmospheric Administration Mg II core-to-wing ratio, derived from the solar Mg II feature at 280 nm, which is a good measure of solar UV and extreme ultraviolet emissions (Viereck & Puga, 1999; Viereck et al., 2001), shows comparable values for both time frames.

The SPICAM data show a sudden increase of the CO_2 number density at $L_s \sim 130°$ (Forget et al., 2009). During this time, Spirit and Opportunity, the two Mars Exploration Rovers, measured a significant and unusual rise of dust opacity, which affected most of the planet (Smith et al., 2006). This increase in optical depth was enough to increase the temperature in the lower atmosphere, thereby raising densities in the upper atmosphere (Forget et al., 2009). However, there are also seasonal variations separate from dust storm influences.

Campaign 7 was executed at $L_s \approx 124°$, shortly before the L_s of $\approx 130°$ at which the storm commenced in MY27, and campaign 8 occurred at $L_s \approx 159°$. Unfortunately, there are no data from the MUV channel for this campaign, which means no CO_2 number densities below about 90 km. However, data from the FUV channel are available for both campaigns. An increase in the IUVS densities can be seen, but it not as distinctive

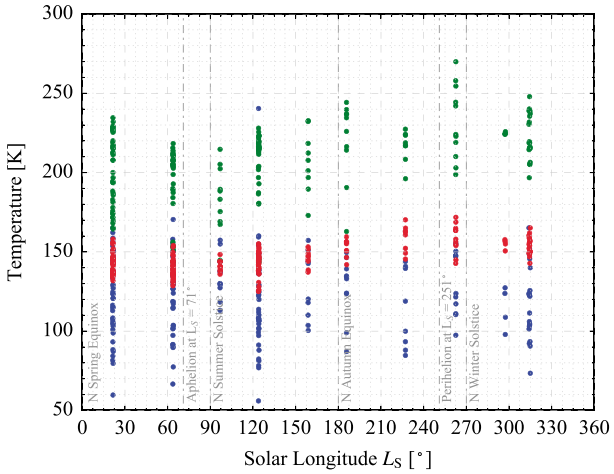

Figure 14. The temperatures required to explain the density variations at 120 km shown in Figure 13. Surface temperatures from the Mars Climate Database are shown in green, temperatures at 120 km inferred from Imaging UltraViolet Spectrograph occultations are shown in blue, and the mean temperature between the surface and 120 km is shown in red.

as in the SPICAM data, especially at $L_s \approx 159°$. Moreover, the IUVS CO_2 number densities from campaign 9, $L_s \approx 186°$, are still slightly lower than the SPICAM values. This suggests that the sharp increase in the SPICAM data near $L_s = 130°$ was due to the dust storm and furthermore that the atmosphere during MY27 remained dustier than during MY33 until at least $L_s = 186°$.

Because the atmosphere is in hydrostatic equilibrium, the variability in CO_2 density at a constant altitude reflects temperature variability at lower altitudes as well as possible variations in the surface pressure. The average temperature in the lower atmosphere can be calculated from hydrostatic equilibrium:

$$\left\langle \frac{1}{T} \right\rangle^{-1} = -\frac{GM}{R_d} \frac{r_0 - r_1}{r_0 r_1} \left(\ln\left(\frac{p_1}{p_0} \right) \right)^{-1}, \quad (21)$$

where G is the gravitational constant, M the mass of Mars, R_d the specific gas constant, r_0 and r_1 the radial distances to the surface and 120-km level along the direction of gravity, and p_0 and p_1 the surface pressure and pressure at 120 km. Because p_0 is not measured in the occulations, values are taken from the MCD for the same geometry as the occultation and for the MY closest in solar flux to the actual flux of the occultations. As mentioned earlier, altitudes used here are relative to the Mars reference ellipsoid, but the MCD altitudes are relative to the areoid (Mars geoid). Thus, to get a comparison in the same altitude space, the MCD altitudes are adjusted to the ellipsoid using a smoothed topography map (based on a $1° \times 1°$ Mars Orbiter Laser Altimeter map). The altitude shift is between −2.52 and 1.12 km. Results for the mean temperature are shown in Figure 14. The observed density variation at 120 km can be explained by a seasonal variation in mean temperature from 140 to 160 K.

4.2. O_3 Density

Ozone on Mars exhibits orders of magnitude variations in space and time as a consequence of photolysis, atmospheric dynamics, and the catalytic destruction cycles induced by hydrogen radicals (HO_x) released by dissociation of H_2O (Lefèvre & Krasnopolsky, 2017). An anticorrelation between O_3 and H_2O is therefore believed to take place in the atmosphere of Mars, and this has been confirmed by spacecraft and Earth-based observations of Mars. As such, O_3 testifies to the oxidizing properties of the Martian atmosphere and returns direct information on the mechanisms at work in controlling the stability of the present-day CO_2 atmosphere.

Ozone is detected only in the MUV channel and only in those occultations that are relatively free of scattered light. This effectively limits O_3 measurements to nightside occultations. Moreover, in some occultations, extinction by aerosols is so large that it masks the O_3 signature. In all, we estimate that we have 163 occultations in which O_3 could be detected if it were sufficiently abundant. We detect O_3 in 70 of these occultations and estimate an upper limit for the remaining 93 occultations. We can measure O_3 for LOS column densities greater than $\sim 10^{15}$ cm^{-2}. Examination of the full set of occultations shows that this upper limit is surprisingly independent of the SNR of the occultation. The peak number density corresponding to this column density limit is $\sim 10^7$ cm^{-3}. We discuss here results from a subset of the observations, concentrating on 18 occultations that yield good altitude profiles of O_3. Table 3 lists the occultations. Our selected observations come from campaigns 3, 5, and 7. These three campaigns are separated by 3 to 4 Earth months, and thus, each campaign represents a different season on Mars: campaign 3 ($L_s \approx 21°$) was executed during early fall in the southern hemisphere (SH), campaign 5 ($L_s \sim 63°$) during late spring in the NH, and campaign 7 ($L_s \approx 124°$) during midwinter in the SH.

The O_3 density profiles for the occultations listed in Table 3 are shown in Figure 15 and compared with the predicted ozone profiles from the MCD. The left panels show the altitude dependence and the right panel the pressure dependence. We show both because altitude is the quantity directly related to the measurements but pressure is more directly related to physical processes in the atmosphere. The pressure corresponding to the O_3 measurement is determined from the CO_2 density and temperature inferred for that altitude.

The retrieved O_3 profiles are generally confined to the ~20- to 60-km region because aerosols usually obscure the O_3 signature at lower altitude while decreasing densities with altitude limit the upper boundary for the

Table 3
Observation Geometry for Occultations Where O_3 Was Detected

Star	Orbit	Campaign	UTC time	Lon (°)	Lat (°)	L_s (°)	SZA (°)	LT (hr)
η UMa	01635	3	1 Aug 2015 - 15:09:17	229.23	−57.50	21.32	123.91	2.42
η UMa	01638	3	2 Aug 2015 - 04:15:15	37.50	−57.44	21.57	124.21	2.40
η UMa	01639	3	2 Aug 2015 - 08:37:15	333.57	−57.41	21.66	124.32	2.38
κ Sco	02132	5	3 Nov 2015 - 20:46:20	331.87	27.81	63.64	114.57	2.88
κ Sco	02133	5	4 Nov 2015 - 01:18:58	265.43	28.07	63.72	114.39	2.88
κ Sco	02134	5	4 Nov 2015 - 05:51:35	199.00	28.59	63.80	113.96	2.89
κ Sco	02135	5	4 Nov 2015 - 10:24:17	132.61	29.14	63.88	113.51	2.89
κ Sco	02136	5	4 Nov 2015 - 14:56:58	66.17	29.52	63.97	113.19	2.89
γ^1 Vel	02848	7	17 Mar 2016 - 12:40:25	236.45	−5.76	123.82	150.91	22.28
γ^1 Vel	02849	7	17 Mar 2016 - 17:10:04	170.53	−5.73	123.91	150.65	22.27
γ^1 Vel	02850	7	17 Mar 2016 - 21:39:42	104.68	−5.71	124.00	150.48	22.25
α Eri	02850	7	17 Mar 2016 - 21:50:31	145.87	−36.75	124.00	157.78	1.17
η UMa	02850	7	18 Mar 2016 - 00:20:48	47.05	−62.07	124.05	128.69	21.05
γ^1 Vel	02851	7	18 Mar 2016 - 02:09:24	38.80	−5.68	124.09	150.26	22.23
α Eri	02851	7	18 Mar 2016 - 02:20:10	80.04	−36.84	124.09	157.82	1.16
η UMa	02851	7	18 Mar 2016 - 04:50:26	341.83	−62.10	124.14	128.83	21.08
γ^1 Vel	02852	7	18 Mar 2016 - 06:39:03	332.90	−5.65	124.18	150.03	22.22
α Eri	02852	7	18 Mar 2016 - 06:49:51	14.21	−36.93	124.18	157.86	1.15

Note. Times and geophysical parameters are given for the half light point of the occultation. SZA = solar zenith angle; LT = local time.

retrievals. There is often an interesting peak in this altitude region that was first observed by Lebonnois et al. (2006), following theoretical predictions of its existence (Clancy et al., 1996; Lefèvre et al., 2004). This peak is seen in the O_3 profiles in panels (c) and (d) for $L_s \approx 63°$ (NH late spring) with a density of $\sim 2 \times 10^9$ cm^{-3} around an altitude of 40 km ($\approx$ 4 Pa), whereas the profiles during the SH midwinter season ($L_s \approx 124°$) show a slightly smaller peak centered at ~30 km. In contrast, the profiles in panels (a) and (b), which represent NH early spring at $L_s \approx 21°$, show constant O_3 densities from around 50 down to 30 km and then an increase at lower altitudes. No clear peak can be seen in these profiles.

The O_3 profiles shown in Figure 15 are consistent with variations observed in prior O_3 measurements. The anticorrelation between O_3 and H_2O, caused by the destruction of O_3 by HO_x radicals, drives much of the O_3 variability (e.g. Lefèvre et al., 2004). The detection of O_3 in the occultations occurs in two areas where the HO_x abundances are small. First, at high southern latitudes in early fall ($L_s \approx 21°$, panels a and b) condensation of H_2O leads to the buildup of large amounts of ozone in the first 30 km above the surface. This observation is consistent with prior detections of O_3 in the southern polar vortex by SPICAM stellar occultations (Lebonnois et al., 2006) and in nadir viewing geometry by SPICAM (Perrier et al., 2006) and MARCI (Clancy et al., 2016). Second, at middle to low latitudes when Mars is near aphelion, we detect a detached layer with a peak near 30 km. This layer of O_3 is due to the fact that the hygropause is quite low near aphelion leading to minimal HO_x and therefore high O_3 densities (Clancy et al., 1996; Lefèvre et al., 2004). The measurements of the detached layer presented here are also mostly consistent with the MEX/SPICAM ozone (Lebonnois et al., 2006). In the first and second IUVS stellar occultation campaigns, performed during the second half of the MY (mean $L_s \approx 315°$ and $L_s \approx 344°$, respectively), no O_3 was detected. This is in agreement with Lebonnois et al. (2006) who only observed O_3 at middle to low latitudes in a period centered on Mars aphelion between $L_s \approx 11°$ and $L_s \approx 130°$. In addition, at middle to low latitudes, we obtain the largest ozone abundances at $L_s \approx 63°$, shortly before the Mars aphelion, and smaller abundances later in the season at $L_s \approx 124°$. This variation also agrees with Lebonnois et al. (2006), who observed a decrease in O_3 in the detached layer starting at a solar longitude of around 100°. Though we see similar seasonal variability, the peak values obtained by Lebonnois et al. (2006) are up to a factor of 5 higher than the values retrieved here.

Our retrieved O_3 profiles also agree fairly well with simulations in the MCD. To perform the comparison, we used the climatology dust scenario, which is a good match for the time of the observations; however, the choice of dust scenario has only a minor effect on the predicted O_3 because there is little O_3 during the dust

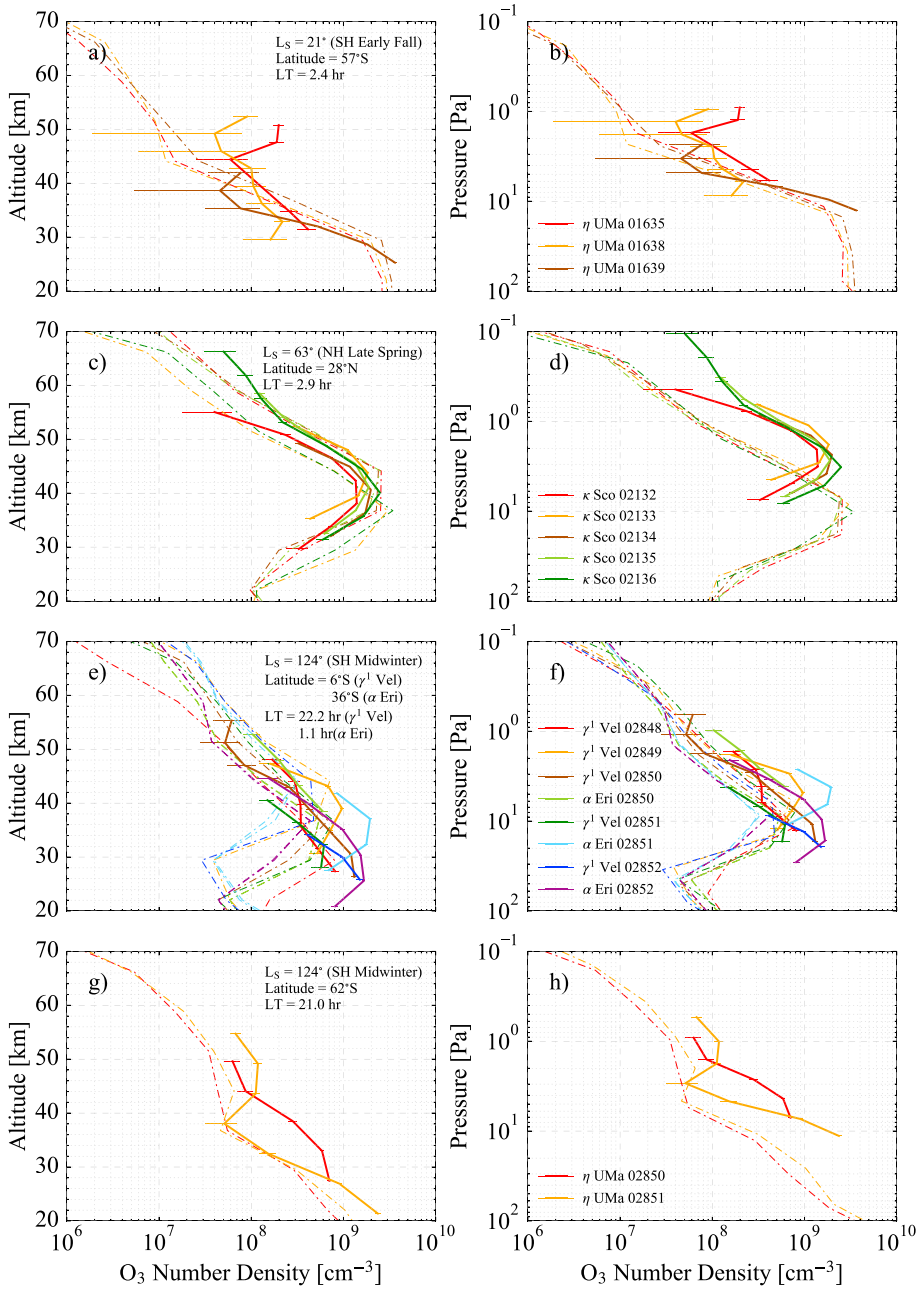

Figure 15. Ozone density profiles for all occultations listed in Table 3. The profiles (a and b) for SH early fall and (c and d) for NH late spring. SH midwinter is shown in panels (e) and (f) for low and middle latitudes and in panels (g) and (h) for high latitudes. In all four cases, the left panel shows the altitude dependence of the ozone profiles and the right panel the pressure dependence. The solid lines represent the Imaging UltraViolet Spectrograph stellar occultation measurements and the dash-dotted lines indicate the predicted ozone profiles from the Mars Climate Database. SH = southern hemisphere; NH = northern hemisphere.

season. The other geophysical variables required to generate MCD profiles (latitude, longitude, local time, etc.) are chosen to be as close as possible to those of the observations. The predicted O_3 density profiles from the MCD agree quite well with those derived from IUVS occultations, although there are some differences (Figure 15). The model captures most of the observed seasonal variation of O_3. Comparing the ozone number density for SH early fall, panels (a) and (b), and SH midwinter low to middle latitudes, panels (e) and (f), show an agreement on both the altitude and the pressure scale. In panels (a) and (b), however, the number densities show differences up to 1 order of magnitude at altitudes higher than 40 km, while for the α Eri

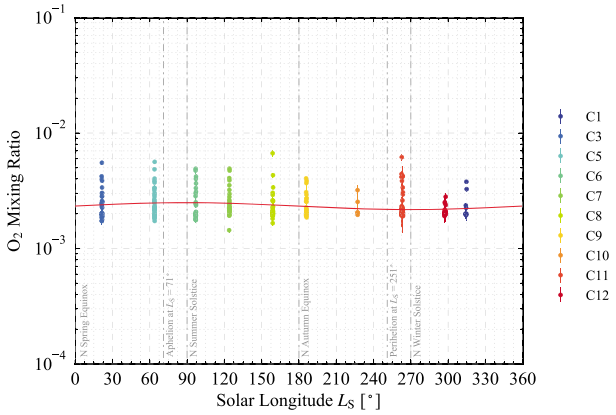

Figure 16. The O_2 mixing ratio at 110 km as a function of L_s. Each color represents data for a different stellar occultation campaign (listed in Table 1). The solid red line shows the sinusoidal least squares best fit including all occultations for the particular altitude. The set of data points at each L_s are for individual occultations, characterized by different latitudes, longitudes, and local times.

(orbit 02851 and 02852) occultations shown in panel (e), the model predicts 1 order of magnitude less O_3 at lower altitudes. There are also significant mismatches between model and data for the η UMa occultations shown in panel (g) and (h). In the case of NH late spring, panels (c) and (d), and the SH midwinter high latitudes, panels g and h, the densities are in agreement on the altitude scale but not on the pressure scale. In both cases, the O_3 abundances obtained from IUVS measurements are at lower pressure, suggesting that the temperature in the MCD model is higher than in the measurements. Nevertheless, the peak number density is comparable, $1-2\times10^9$ and $2-3\times10^9$ cm^{-3} for IUVS measurements and MCD data, respectively. The other discrepancies mentioned above indicate shortcomings of the model and merit further, in-depth investigation but are outside the scope of this paper.

4.3. O_2 Density

Measurement of O_2 indicates the oxidizing capacity of the atmosphere and provides an additional constraint on the oxygen chemistry. As the chemical lifetime of O_2 is large (60 Earth years), it constrains the oxygen chemistry over much longer timescales than does O_3. With the few previous O_2 observations, IUVS opens up an era of systematic tracking of O_2 above 90 km.

The first O_2 measurements used the A band absorption at 763.5 nm for the detection with Earth-based telescopes (Barker, 1972; Carleton & Traub, 1972; Trauger & Lunine, 1983). In the same time frame, Nier and McElroy (1977) used the Viking mass spectrometer to determine an O_2 mixing ratio of 10^{-3} in the altitude range between 110 and 180 km. Recently, O_2 was detected the first time in the millimeter wavelength range by Hartogh et al. (2010) using the high-resolution spectrometer Heterodyne Instrument for the Far Infrared of the space observatory Hershel. They determined a mole fraction of $1.40\pm0.12\times10^{-3}$ averaged over altitudes between the surface and 100 km and the disk. A similar O_2 mole fraction of $1.45\pm0.09\times10^{-3}$ at the surface is obtained by Mahaffy et al. (2013) using Surface Analysis at Mars on the Curiosity rover. The most extensive O_2 measurements to date come from the UV occultation experiment on MEX, using a technique similar to that employed here. Sandel et al. (2015) derived O_2 mixing ratios from 6 MEX/SPICAM UV occultations and derived mixing ratios from 3.1 to 5.8×10^{-3} for different occultations.

The O_2 mixing ratio at 110 km derived from the MAVEN UV occultations is shown as a function of L_s in Figure 16. The mean value of the O_2 mixing ratio is 2.5×10^{-3}, consistent with the results of Sandel et al. (2015). This is significantly larger than the Viking value. It is unclear whether this reflects a change in the atmosphere or difference in observational techniques. The mean mixing ratio is also significantly larger than the near-surface values mentioned above. An increasing mixing ratio with altitude is expected for a photochemical constituent produced in the upper atmosphere; however, this trend is opposite to that required by Hartogh et al. (2010) to fit their line profile measurements. A least squares fit of a sinusoidal to the data indicates less than 50% variation with season, but the variability at any given solar longitude is much larger, with values that range from 1.5×10^{-3} to 6×10^{-3} at 110 km. The strong variability of the O_2 mixing ratio likely reflects a complex variation with latitude and local time. With the small number of samples to date, it is impossible to discern these variations directly from the data, but the measurements can provide strong constraints on Global Climate Model (GCM) simulations of the O_2 distribution.

4.4. Temperatures

The measured temperature profiles for λ Sco shown in Figure 17 are in rough agreement with the MCD profiles for pressures between 10^{-4} and 10 Pa. The disagreements at high pressure could be due to confusion between aerosol and CO_2 signatures in the observations, and we do not consider the differences to be significant. At low pressure, the MCD model temperatures are up to 40 K warmer than the measurements. Previously, Forget et al. (2009) and Gröller et al. (2015) noted that predictions from the LMD-MGCM were tens of kelvins less than observed temperatures at pressures less than $\approx10^{-4}$ Pa. The same disagreement was seen with MGCM-MTGCM simulations (McDunn et al., 2010). Forget et al. (2009) and McDunn et al. (2010) suggested that the disagreement was due to an inaccurate description of radiative balance in the GCM simulations. Upgrading the LMD-MGCM (Gonzalez-Galindo et al., 2009) to calculate O densities in a self-consistent manner

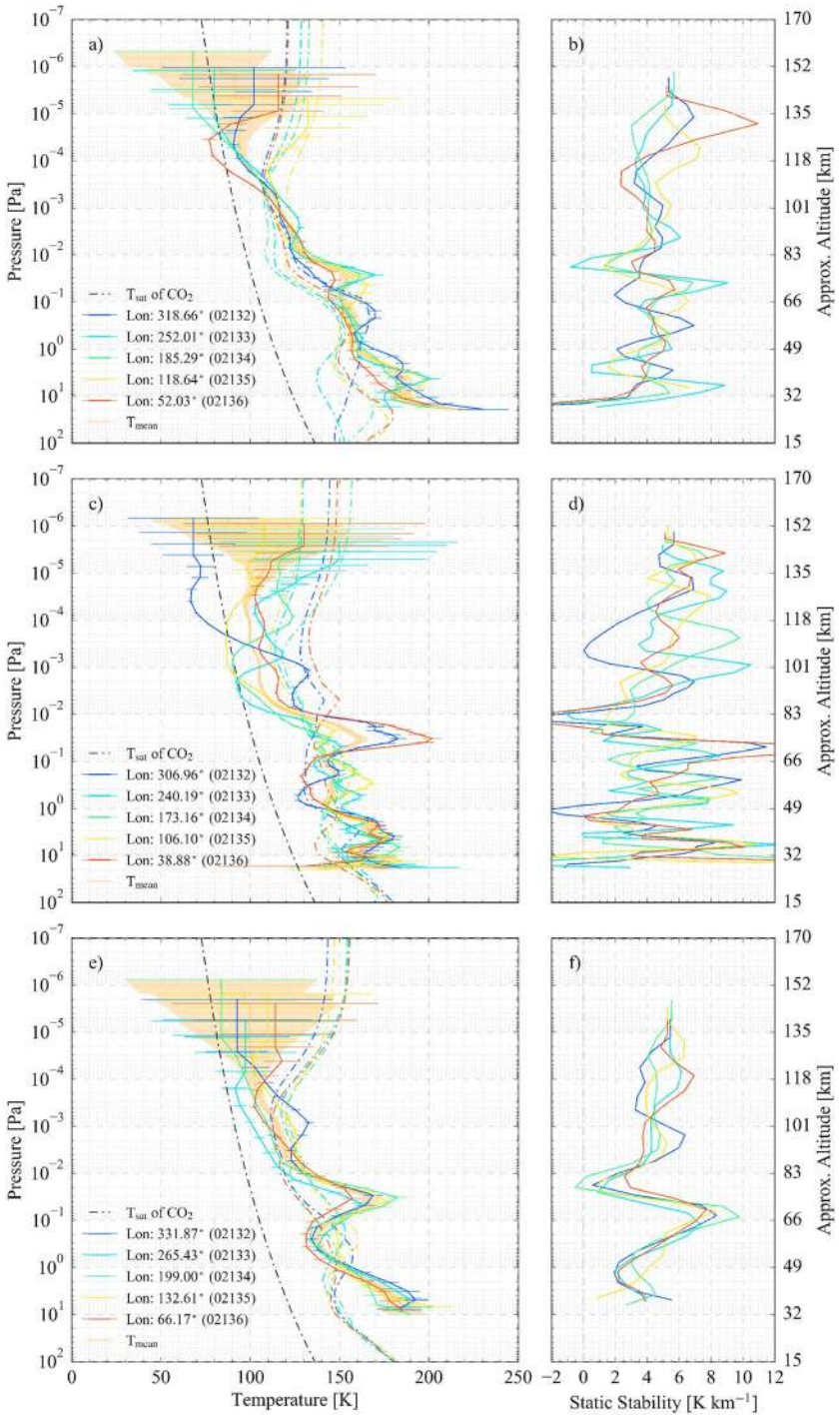

Figure 17. Longitude variability of the temperature profiles for three different stars during campaign 5. The left panels show the temperature profiles from the Imaging UltraViolet Spectrograph instrument (solid lines) and predicted values from the Mars Climate Database (dash-dotted lines). The black dash-dotted line indicates the CO_2 saturation temperature. The mean value temperature profiles including uncertainties is shown in orange. The right panels show the static stability, the difference between the environmental, and the adiabatic temperature gradient. (a and b) The λ Sco (Lat = −56.20°, LT = 1.07 hr, SZA = 144.30°), (c and d) α^1 Cru (Lat = 2.19°, LT = 2.06 hr, SZA = 141.01°), and (e and f) κ Sco (Lat = 29.52°, LT = 2.89 hr, SZA = 113.19°).

Table 4
Observation Geometry for Dayside Occultations

Star	Orbit	Campaign	UTC time	Lon (°)	Lat (°)	L_s (°)	SZA (°)	LT (hr)
γ^1 Vel	03489	9	14 Jul 2016 - 18:43:56	45.27	10.89	185.75	17.08	11.28
α Pav	03489	9	14 Jul 2016 - 20:05:46	26.65	−63.04	185.78	61.03	11.38
α Pav	03490	9	15 Jul 2016 - 00:30:39	321.34	−62.75	185.89	60.78	11.32
γ^1 Vel	03491	9	15 Jul 2016 - 03:33:44	275.76	10.91	185.96	17.51	11.24
γ^1 Vel	03492	9	15 Jul 2016 - 07:58:38	211.03	10.91	186.07	17.72	11.23
γ^1 Vel	03493	9	15 Jul 2016 - 12:23:34	146.23	10.92	186.17	17.97	11.21

Note. Times and geophysical parameters are given for the half light point of the occultation. SZA = solar zenith angle.

improved the agreement between models and SPICAM observations substantially in the 10^{-4}- to 10^{-3}-Pa region (Montmessin et al., 2017). The improved description of the O chemistry and diffusion resulted in higher O densities and larger radiative cooling due to O-CO_2 collisions, lowering the temperatures in the LMD-MGCM simulations. The results presented here show that the GCM predictions are still warmer than observations in the 10^{-6}- to 10^{-4}-Pa region. This may indicate that the radiative balance is not adequately described in this pressure region. Alternatively, the disagreement could be due to an underestimation of cooling due to gravity waves, which has been shown to be important in the Earth's upper atmosphere (Walterscheid, 1981; Yiğit & Medvedev, 2009). The LMD-MGCM used to produce the MCD includes parametrization of the effect of the gravity waves induced by the wind flowing over the orography (Angelats i Coll et al., 2005; Forget et al., 1999) but do not represent the possible gravity waves produced by nonorographic sources, such as convection or fronts. The intensity of the nonorographic sources is not well constrained, but the effects have been explored by the Max-Planck-Institut (MPI)-MGCM model (Medvedev et al., 2011). The cooling due to these waves is potentially strong enough to explain the temperature differences shown here (Medvedev & Yiğit, 2012), but a detailed comparison with MAVEN results has yet to be performed. The relative merits of the radiative cooling and gravity wave cooling hypotheses as manifest in the MPI-MGCM have been discussed by Medvedev et al. (2015). In general, gravity waves tend to cool at lower pressures than do radiative emissions. Detailed comparisons between these models and the observations described here may help to settle this question.

The observed profiles exhibit periodic perturbations with scale lengths of 10–30 km and amplitudes of up to 50 K. These are likely the signatures of tides or waves in the atmosphere. The perturbations exhibit a variety of behaviors. For example, the wave-like structure seen at lower altitudes in the κ Sco measurements is largely in phase for the longitudes sampled, suggesting that this is a migrating tide, that is, fixed in local time. The perturbations seen in the α^1 Cru occultations show less correlation with longitude, suggesting that these may be the signatures of nonmigrating tides and/or gravity waves. Evidence for nonmigrating tides in the IUVS occultation data is discussed further in the next section.

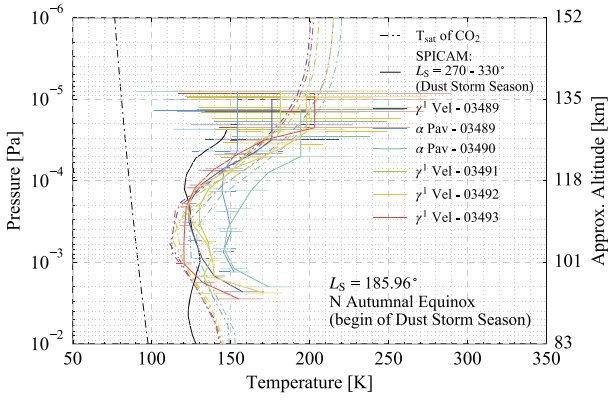

Figure 18. Dayside temperature profiles (solid lines) at around 11:30 local time at the beginning of the dust storm season; each color represent a different stellar occultation. The colored dash-dotted lines illustrate the temperature profiles taken from the Mars Climate Database (MCD) and the black dash-dotted line indicates the CO_2 saturation temperature. The black solid line indicates the dayside temperature recorded with SPICAM from Forget et al. (2009).

The large perturbations in the α^1 Cru and κ Sco temperature profiles are sometimes below the CO_2 condensation point, implying that CO_2 is supersaturated at these locations. These phenomena were seen previously in temperature profiles retrieved from SPICAM occultation measurements (Forget et al., 2009). There are extensive discussion in the literature about the relationship of these cold pockets to the mesospheric CO_2 clouds (Listowski et al., 2014; Määttänen et al., 2010; Montmessin, Bertaux, et al., 2006; Spiga et al., 2012; Yiğit et al., 2015). At these low pressures, the cloud particles must be small to remain aloft and therefore are most easily observed in the UV. In fact, this phenomenon was also observed with SPICAM/UV and Montmessin, Bertaux, et al. (2006) showed that temperatures below the CO_2 condensation point were sometimes associated with detached clouds. There is no evidence for detached clouds in the MAVEN data shown here, but the sample size is still small. The IUVS occultation results cover a larger-altitude range than previous measurements. An examination of the profiles in Figure 17 strongly suggests that the cold pockets are due to tides or waves in the atmosphere with the overall

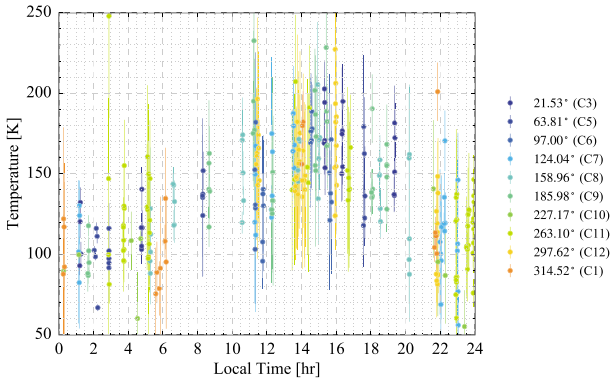

Figure 19. Local time dependency of the retrieved temperatures at a pressure level of 3×10^{-5} Pa (around 125 km) and for latitudes below 50°. Colors represent different solar longitudes L_s as indicated in the legend with the corresponding campaign number given in parentheses.

decrease in temperature with altitude combined with the increasing amplitude with altitude, as originally suggested by Clancy and Sandor (1998) and assumed in numerous subsequent studies.

Figures 17b, 17d, and 17f show the static stability for the three temperature profiles shown in Figures 17a, 17c, and 17e. The temperature profile becomes unstable near 10^{-2} Pa in the α^1 Cru occultations for three of the individual profiles and close to unstable for the other two. A similar but weaker feature appears at the same pressure in the λ Sco and κ Sco profiles. The feature appears at all longitudes, suggesting that it could be a migrating tide that breaks near this level of the atmosphere. The fact that the atmospheric stability is low near 10^{-2} Pa for all three profiles suggests that this may be a widespread phenomenon at least in late northern spring on Mars. Examination of more data to understand the frequency and geographic distribution of these features is required to investigate further.

We have obtained over 100 dayside results where the stray light does not directly interfere with the recorded stellar signal in the FUV channel. Around 50 occultations have been recorded between 10:00 and 14:00. The geometry for some occultations around noon is listed in Table 4, and results are shown in Figure 18 for eight occultations (solid line) including their comparison with the MCD (dash-dotted lines) and the CO_2 saturation temperature (black dash-dotted line). In addition, the dayside temperature profile from Forget et al. (2009) is included as a black solid line. This profile is an average of four profiles, recorded with the SPICAM instrument between 10:00 and 15:00 at a latitude between 40°N and 50°N and a solar longitude between 270° and 330° during the dust storm season. No IUVS stellar occultations are available for the latitudes and local times mentioned in Forget et al. (2009); thus, no direct comparison of the dayside temperatures from MEX/SPICAM and MAVEN/IUVS can be done. In general, the dayside temperatures from the MCD are lower than the temperatures retrieved from the IUVS instrument. The temperature difference varies from around 10 up to almost 50 K. However, the altitude of the temperature minimum seems to be in agreement. This is not true for the SPICAM profile, which is closer to the MCD profiles but shows a minimum at a substantially lower pressure.

Figure 19 shows the variation of temperature with local time for a pressure level of 3×10^{-5} Pa (around 130 km) and for latitudes below 50°. There is a clear diurnal variation with a minimum temperature of ~100 K from midnight to ~04:00 and broad maximum of ~170 K in the early afternoon from noon to ~16:00. The relatively large variability about this diurnal variation could be due to variations with latitude and season. These are the first observational constraints for diurnal temperature variations at this level of the atmosphere.

4.5. Wave Structures

Tides in the Mars thermosphere have large amplitudes and have significant effects on the energy and momentum balance (Moudden & Forbes, 2008). The most recent occultation campaigns that target a given star for 10 different longitudes provide an excellent data set for the study of nonmigrating tides. In general, tidal oscillations can depend upon both local time and longitude as well as altitude and latitude and will vary with season. The local time and longitude dependence of a tide can be expressed as a Fourier series in the local time t_{LT} frame as

$$\frac{\Delta N}{N} = \sum_n \sum_s A_{n,s}(z,\Theta)\cos\left(n\Omega t_{LT} + (s-n)\lambda - \Phi_{n,s}(z,\Theta)\right), \tag{22}$$

where n is a positive integer denoting the subharmonic of the solar day ($n = 1$ for diurnal tides, $n = 2$ for semidiurnal tides, and so on), s the zonal wave number is also an integer with negative (positive) values denoting an eastward (westward) propagating waves, λ is the longitude, and Ω the planet rotation rate. The amplitude $A_{n,s}$ of the harmonics and the phase $\Phi_{n,s}$ are altitude z and latitude Θ dependent. For the discussion of tides it is also useful to define the apparent zonal wave number in local time frame $m = s - n$. Migrating tides have $s = n$ and $m = 0$ and are therefore independent of longitude but move with the Sun. For nonmigrating tides, $s \neq n$ and $m \neq 0$. As the occultation measurements occur at a fixed t_{LT}, only nonmigrating tides

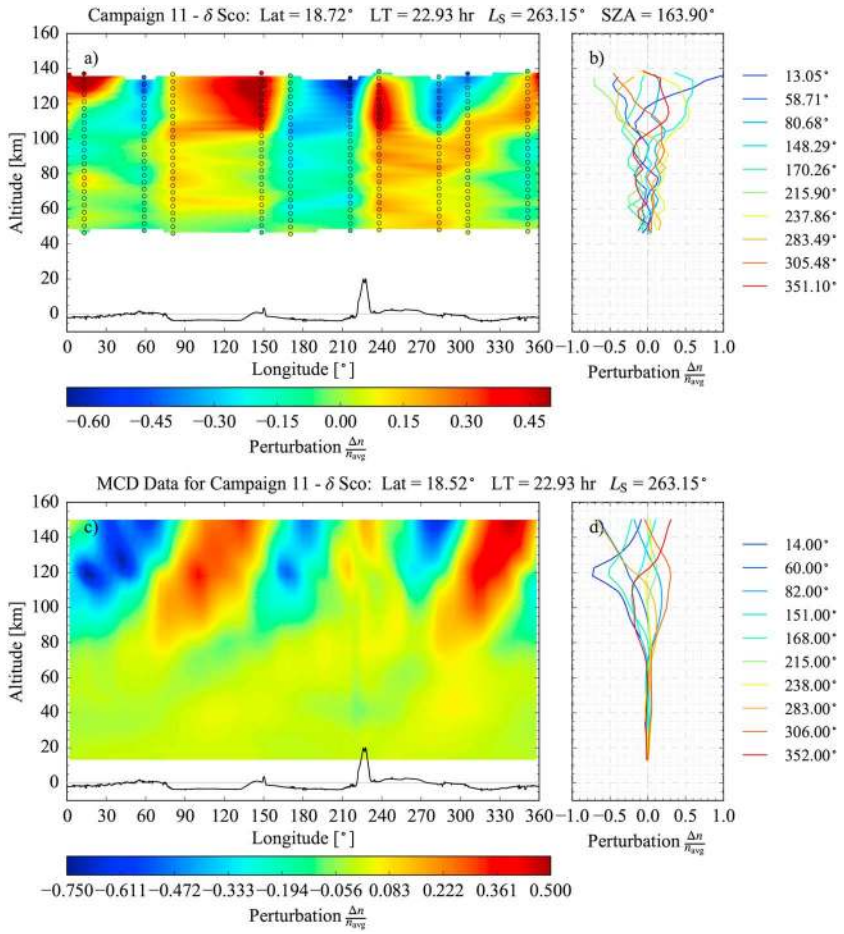

Figure 20. (a and b) The perturbations in the CO_2 number density using occultations from 10 consecutive orbits targeting δ Sco during campaign 11 at a latitude of 18.72°N and a local time of 22.93. (c and d) The perturbations in the number density obtained from the Mars Climate Database (MCD) for the same geometry as the Imaging UltraViolet Spectrograph stellar occultations shown in the top row. The density perturbations are defined as the difference between the local measurement and the mean in longitude at that altitude divided by the longitude mean. Linear interpolation between the data points is used to create the image. Circles represents the location of the measurements. The solid line at the bottom of the image shows the topographic profile of the Martian surface at 18.72°N, with Olympus Mons at around 230°E. Panels (b) and (d) show the altitude profile of the perturbations for each occultation at the longitudes listed.

are measured. Nonmigrating tides can be generated by various mechanisms, including nonlinear interactions between the westward propagating migrating tides directly forced by the Sun and the surface (topographic height and roughness, surface thermal inertia and albedo), zonally asymmetric dust distributions, and nonlinear coupling between migrating tides and stationary planetary waves (Angelats i Coll et al., 2004; Forbes et al., 2002). Previous observations indicate that the most prominent nonmigrating tides on Mars have apparent zonal wave numbers of $m = 2$ and 3 (e.g. Angelats i Coll et al., 2004; Forbes et al., 2002; Wilson, 2002). A variety of combinations of s and n can lead to apparent $m = 3$ tides in the local time frame, for example, an eastward propagating diurnal $n = 1$ oscillation with a zonal wave number $s = -2$ (referred to as DE2), or an eastward propagating semidiurnal $n = 2$ oscillation with a zonal wave number $s = -1$ (referred to as SE1). The main contribution to $m = 2$ nonmigrating tides are an eastward propagating diurnal $n = 1$ oscillation with a zonal wave number $s = -1$ and a standing semidiurnal $n = 2$ with a zonal wave number $s = 0$.

Figures 20a and 20b show the CO_2 number density perturbations retrieved from the occultations of δ Sco during campaign 11. These occultations occurred at a mean latitude of 18.72°N, a mean local time of 22.93,

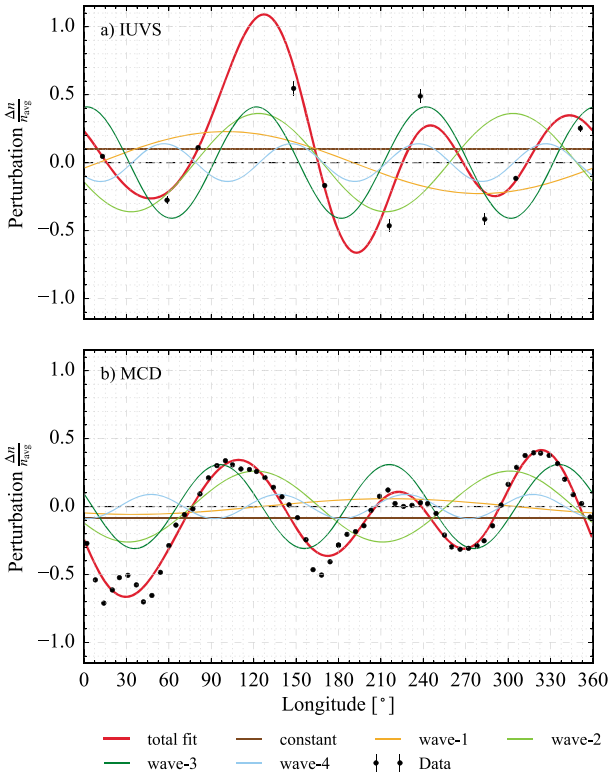

Figure 21. Harmonic fit of the number density perturbations at 120 km altitude for IUVS stellar occultations (panel a) and at 122.65 km for the MCD simulation at the same geometry (panel b). Black solid circles represent the data from measurements and from the model. The red line shows the total harmonic fit, including the first four harmonics. IUVS = Imaging UltraViolet Spectrograph; MCD = Mars Climate Database.

and $L_s = 263°$. Highly structured perturbations throughout the observed region can be seen dependent on altitude and longitude. The structure below 100 km is quite complex, but above 100 km the perturbations are dominated by $m = 3$ tides. The perturbations relative to the zonal mean ($\Delta N/N$) are 50% or more at altitudes above 125 km. The peaks in ($\Delta N/N$) are roughly equally spaced (within tens of degrees) with one peak near 240° longitude close to the Tharsis region and another peak near 150° over the Elysium region. We emphasize that this longitudinal wave pattern is derived from a sequence of independent occultation measurements. Figure 21a shows the density perturbations at 120 km along with a least squares fit to a Fourier series (i.e. equation (22). The fit yields perturbation amplitudes of $\Delta N/N = 0.22 \pm 0.22, 0.33 \pm 0.21$, and 0.41 ± 0.18 for the $m = 1$, 2, and 3 components, respectively.

Figures 20c and 20d show MCD simulations for the same geometry as the IUVS stellar occultations. The altitude profile of the perturbations shown in panel (d) is for the longitudes that are closest to the measurements (shown in panel b). The MCD results are similar to the observations in several ways. In both cases the perturbation amplitudes grow with altitude, reaching roughly 50% in the upper thermosphere. At these high altitudes both observations and models appear to be dominated by an $m = 3$ tide. Even the phases are similar with peaks near 130°, 230°, and 350° longitude. There are some differences as well. The maximum near 230° is much stronger in the observations than the MCD and generally the wave structures appear more tilted in altitude-longitude space in the MCD than in the data. A spectral fit to the perturbations at 122.65 km is shown in Figure 21b. The amplitudes of the $m = 1$, 2, and 3 waves are 5.8×10^{-2}, 2.6×10^{-1}, and 3.1×10^{-1}. The $m = 2$ and 3 amplitudes are similar to the values listed above for the fit to the observations. Figures 20c and 20d show a monthly average of the density structure at a given local time predicted by the MCD and therefore tides appear clearly because less regular structures, such as traveling waves, are averaged out. The MCD also provides an estimation of the day-to-day variability and indicates that traveling waves may significantly contribute to the instantaneous density field observed by IUVS and explain some of the difference between

Table 5
Parameters From the Fit of Density Perturbations at 122.65 km to Zonal Harmonics

n	s	m	$A_{n,s}$	$\Phi_{n,s}$
1	−2	−3	2.21×10^{-1}	67.68
1	−1	−2	1.69×10^{-1}	94.66
2	0	−2	6.77×10^{-2}	91.02
2	−1	−3	5.80×10^{-2}	−17.18
2	−2	−4	4.97×10^{-2}	140.96
2	1	−1	4.40×10^{-2}	−21.19
1	−3	−4	3.95×10^{-2}	157.37
1	0	−1	3.57×10^{-2}	143.09
0	1	1	3.54×10^{-2}	164.46
0	3	3	2.20×10^{-2}	−17.69
1	4	3	2.09×10^{-2}	−69.01

Note. $A_{n,s}$ is the amplitudes and $\Phi_{n,s}$ the phases determined in the fit.

the measurements and the model shown in Figure 20. The clear tidal signature in the δ Sco occultation may indicate weak contributions of other wave modes for the particular time and place of the measurement. It is, in fact, rare to see such a clear tidal signature in a single set of measurements. Detailed examination of more data is required to determine the relative importance of tides and other waves in the average atmosphere.

The stellar occultations shown in Figure 20 are recorded at a single local time (22.93 hr) and so cannot be used to separately determine s and n; however, given the similarity between the MCD simulation and the observations, it is instructive to examine the local time behavior of the tides in the MCD. By fitting the density perturbations in the MCD model to equation (22) we can determine the amplitude $A_{n,s}$ and phase $\Phi_{n,s}$ of the harmonics. Results are shown for the 122.65-km level in Table 5. To perform the fit, we use all combinations between the wave numbers n and s that produce zonal wave numbers $m \leq 4$. According to the fit, perturbations seen in the MCD data are a combination of stationary waves ($n = 0$), eastward and westward propagating nonmigrating tides ($s \neq n$ and $m \neq 0$), and migrating tides ($m = 0$). The main contributions to the perturbations seen in the MCD data, in decreasing order, are a diurnal eastward propagating wave-3 ($n = 1$ and $s = -2$), a diurnal eastward propagating wave-2 ($n = 1$ and $s = -1$), a semidiurnal standing wave-2 ($n = 2$ and $s = 0$), and a semidiurnal eastward propagating wave-3 ($n = 2$ and $s = -1$).

Previously, Lo et al. (2015) and Medvedev et al. (2016) have discussed nonmigrating tides observed in MAVEN/IUVS airglow observations, while England et al. (2016) have analyzed both MAVEN airglow measurements and mass spectrometer measurements. The airglow observations cover the altitude range from 130 to 180 km and therefore just overlap with the uppermost altitudes in the occultation retrievals. The Neutral Gas Ion Mass Spectrometer observations analyzed by England et al. (2016) sample the 165- to 205-km region. Lo et al. (2015) and Medvedev et al. (2016) analyzed data from October 2014 for which L_s ranged from 216.7° to 218.9° and local time from 13:40 to 15:00. England et al. (2016) analyzed data from April 2015 for which $L_s = 318.1$ to 319.5°.

Lo et al. (2015) determined amplitudes of $19 \pm 3\%$, $16 \pm 2\%$, and $9 \pm 2\%$ for the $m = 1$, 2, and 3 components of the perturbations from the zonal mean. These amplitudes are derived from fits assuming a Chapman profile for the volume emission rate (VER) over the altitude range of the emissions. The peak altitude of the VER is a fit parameter and derived values are in the 125- to 135-km region; therefore, the resulting perturbation amplitudes are most strongly weighted by variations near this altitude region. By examining the latitudinal variations in wave amplitude Lo et al. (2015) argued that the $m = 3$ component was due primarily to DE2 tide with a contribution from SE1 enhancing amplitudes at low latitudes. This is consistent with Withers et al. (2011) who analyzed tidal signatures in densities from SPICAM/UV occultations and concluded that SE1 dominated at low latitudes and DE2 at high latitudes. England et al. (2016) also derived tidal variations from the VER but concentrated on higher altitudes, from 165 to 195 km. They find wave amplitudes of 15% for $m = 2$ and ≈5% for $m = 1$ and $m = 3$, quite similar to the value in Lo et al. (2015). The wave amplitudes in the δ Sco observations are significantly larger, with the $m = 3$ tide nearly a factor of 10 greater.

Medvedev et al. (2016) concentrated on a latitude band near 19.4°N, which is similar to that for the δ Sco occultation analyzed here. In contrast with Lo et al. (2015) and England et al. (2016), but consistent with the results reported here, they find that longitude perturbations are dominated by $m = 3$. No Fourier analysis is presented in the paper, and this statement is based on visual inspection of Figure 3 of Medvedev et al. (2016). The perturbation amplitudes calculated by Medvedev et al. (2016) appear to be approximately a factor 2, significantly larger than found by Lo et al. (2015) and England et al. (2016) but consistent with the δ Sco occultation results. The different conclusions about the relative importance of $m = 2$ and $m = 3$ tides in Lo et al. (2015) and Medvedev et al. (2016) from the same data set may be related to that fact that Lo et al. (2015) based their analysis on the peak altitude of the observed intensities, whereas Medvedev et al. (2016) relied on the CO_2 densities derived from the emissions. In principle, these two approaches should give the same results and the differences between Lo et al. (2015) and Medvedev et al. (2016) merit further investigation. It is worth

noting that the coverage of the emission and density data sets differ because not all emission profiles can be confidently converted to density.

Medvedev et al. (2016) also present simulations from the MPI-MGCM for the same season and solar activity as the October 2014 IUVS emission data. The simulations predict that the thermosphere is dominated by a $m = 3$ tide and that this tide is stationary ($s = 0$) and extends from the surface to the thermosphere. The amplitude of the tide appears to be roughly a factor of 2. Thus, the wave number and amplitude of the tide in the MPI-MGCM simulations are consistent with the results reported here, albeit with a significantly different phasing: the occultations have a maximum density near black240°E longitude, while the MPI-MGCM simulations predict a minimum. We note, however, that the δ Sco occultation occurred at a significantly different L_s than the Medvedev et al. (2016) simulations. With the information available we cannot present a detailed comparison of the MPI-MGCM and MCD simulations.

Previously, Keating et al. (1998) suggested the important of stationary Rossby waves in the Mars thermosphere on the basis of accelerometer measurements made on board the Mars Global Surveyor spacecraft. Subsequently, Forbes and Hagan (2000) and Joshi et al. (2000) showed that these signatures were likely due to nonmigrating tides rather than stationary tides. More detailed comparison with the LMD-MGCM confirmed this (Angelats i Coll et al., 2004). The calculations in Medvedev et al. (2016) show that the $n = 3$ stationary tides can propagate to high altitudes. The source of the tide is not clear. It could be forced by the $m = 3$ component of the surface topography or by nonlinear wave interactions in the lower atmosphere (Medvedev et al., 2016). As our spectral analysis shows the tide in the MCD simulations is not stationary but rather a combination of $s = 1$ and $s = 2$ tides. This difference between the MCD results and MPI-MGCM simulation deserves further investigation.

In summary, the δ Sco occultation shows a strong $m = 3$ tide in the thermosphere and Fourier analysis indicates the presence of weaker $m = 1$ and $m = 2$ tides as well. The amplitude of all tidal components is significantly larger than that found in the Lo et al. (2015) and England et al. (2016) analyses of MAVEN/IUVS airglow observations obtained earlier in the mission. It is unclear if this difference is due to the different observational technique or represents real variability in the atmosphere. Comparison with MCD simulations for the same geometry and similar solar conditions shows good agreement in both amplitude and phase with the observations. Calculation of tidal perturbations using the MPI-MGCM (Medvedev et al., 2016) predicts strong $m = 3$ stationary tides that agree qualitatively in amplitude but not phase with the occultation results but the implications of this are not clear because the simulations are for a substantially different L_s. The MPI-MGCM simulations are in qualitative agreement with the Medvedev et al. (2016) analysis of density perturbations derived from IUVS airglow observations but not with the more direct analysis of perturbations in airglow emissions derived by Lo et al. (2015) and England et al. (2016). Resolution of these somewhat confusing and contradictory results requires investigation of the systematic biases for the observational characterization of the tides, a more careful and sophisticated comparison of models and data, and, most importantly, analysis of the full set of MAVEN observations of thermospheric tides.

5. Summary and Conclusions

At the time of writing MAVEN has executed 12 campaigns, yielding 406 FUV and 163 MUV occultations of good quality. From these measurements, we are able to retrieve CO_2, O_2, and O_3 number densities profiles and, assuming hydrostatic equilibrium, temperature profiles. Combining the FUV and MUV channels, CO_2 density profiles and temperature profiles can often be obtained for altitudes ranging from around 20 km up to almost 160 km, covering 7 orders of magnitude in pressure from $\sim 2 \times 10^1$ Pa to $\sim 4 \times 10^{-7}$ Pa. O_3 profiles are confined to the lower atmosphere, typically from 20 to 60 km or $\sim 3 \times 10^1$ Pa to $\sim 3 \times 10^{-1}$ Pa. O_2 profiles are confined to the upper atmosphere, typically from around 90 to 150 km or 10^{-2} Pa to 10^{-6} Pa. The occultation observations to date cover a full MY, MY33, and sample the full range of longitudes and latitudes from 80°S to 75°N. Local times are densely sampled on the nightside of the planet. Contamination of the data by stray light often plagues dayside occultations; nevertheless, we have been able to obtain good results for over 100 dayside occultations; around 50 occultations are recorded between 10:00 and 14:00 local time. These data have led to a number of significant science results.

Our analysis shows that CO_2 densities vary seasonally in rough agreement with the SPICAM results presented in Forget et al. (2009) but absent the signature of the large dust storm that began at $L_s = 130°$ during MY27.

Assuming that the seasonal variation in CO_2 density at 120 km is driven by changes in the temperature of the lower atmosphere implies a variation of 20 K for the mean temperature between the surface and 120 km.

The occultations analyzed here represent the most extensive set of measurements to date of the O_2 density in the Martian upper atmosphere. We find a mean mixing ratio at 110 km of 2.5×10^{-3}. This is consistent with the range found by Sandel et al. (2015) from SPICAM/UV occultations but significantly larger than the previously accepted value of 10^{-3}. The O_2 mixing ratio is variable about this mean, with values ranging from less than 1.5×10^{-3} to 6×10^{-3} at 110 km. The cause of the variability is not well understood at this time. The variation in mixing ratio is not simply related to any individual geophysical variation (latitude, longitude, and season) but is likely related to complex circulation patterns in the Martian atmosphere.

Our O_3 observations pertain primarily to the detached layer in the 20- to 60-km region as high aerosol optical depth usually prevents the analysis of data at lower altitudes and ozone densities are quite small at altitudes above 60 km. Ozone densities are also highly variable, as expected based on previous measurements. Comparison with simulations made using the MCD shows that the model captures the seasonal variations of O_3 quite well. We observe large O_3 densities in the winter polar regions and in midlatitudes when Mars is near aphelion. In most cases the altitude profiles agree quite well with the model predictions, but in some cases the pressure scale differs by a substantial amount. The reason for this discrepancy is still under investigation.

The occultations yield temperature profiles from pressures greater than 10 to less then 10^{-6} Pa. Results are similar to previous measurements, including the discrepancy between the inferred profiles and model simulations in the 10^{-3}- to 10^{-5}-Pa range. In fact, because of the large-altitude range covered by the results presented here we provide better definition on this discrepancy than has been previously available. Observed temperatures near 10^{-4} Pa can be up to 40–50 K cooler than predicted by MCD simulations. Temperatures in this region are often below the condensation point of CO_2, confirming results derived from SPICAM/UV occultations. To date, however, we have not observed a correlation between these cold patches and detached clouds, as was found in the SPICAM data (Montmessin, Bertaux, et al., 2006). Comparison of these profiles with models may illuminate the relative roles of enhanced CO_2 radiative cooling and gravity wave cooling in causing the low temperatures Yiğit et al. (2015). We also derive several dayside temperature profiles that appear to be consistently warmer near 5×10^{-4} Pa, by tens of kelvins, than predicted by the MCD.

The CO_2 density profiles also exhibit quasiperiodic perturbations that are the likely signature of waves in the atmosphere. The spectrum of waves includes tides with periods that are subharmonics of the Martian day and smaller-scale gravity waves that are not so tightly coupled to the planetary rotation. Examination of longitudinal variability in the equatorial region near northern winter solstice, measured in repeated occultations of a given star during a campaign, reveals strong nonmigrating tides in the thermosphere. The perturbations are dominated by zonal wave numbers 2 and 3 and have an amplitude of greater than 45%. This is consistent with MCD simulations, which also agree with the phase of the observed perturbations. Spectral analysis of the MCD simulations implies that the observed perturbations could be due to a combination of diurnal wave combined with $s = -1$ and $s = -2$ longitudinal waves.

All of the topics discussed here, CO_2 seasonal variations, O_2, and O_3 altitude profiles and seasonal/latitudinal variations, vertical temperature profiles, and wave and tide signatures merit further investigation that can be accomplished with a more detailed examination of the occultation results. The description of experiment, reduction procedures, and the initial results presented here should facilitate these future investigations.

Appendix A: UV Star Catalog

The star catalog used to select stars for IUVS stellar occultations is based on observations from SPectroscopy for Investigation of Characteristics of the Atmosphere of Mars on board of MEX (SPICAM), SPectroscopy for Investigation of Characteristics of the Atmosphere of Venus on board of Venus Express, International Ultraviolet Explorer (IUE), and Orbiting Astronomical Observatory-2. A comparison of stellar spectra obtained from the SORCE/SOLSTICE with IUE and MEX/SPICAM are discussed in Snow et al. (2013). Table A1 lists the first 70 stars of the catalog used for IUVS stellar occultations, according the their 150-nm brightness, including their HD (Henry Draper Catalogue) and HR (Yale Bright Star Catalogue) number, the ranking according to their 250-nm flux, their RA, DEC, spectral type, and visual magnitude m_V. The last column in this table lists the source for the flux values.

Journal of Geophysical Research: Planets

10.1029/2017JE005466

Table A1
UV Star Catalog Used for IUVS Stellar Occultations

Rank					Right ascension	Declination			Flux at 150 nm	Flux at 250 nm	
150 nm	250 nm	HR	HD	Name	(hr min s)	(°)	Spectral type	m_V	(photons $cm^{-2} \cdot s^{-1} \cdot nm^{-1}$)	(photons $cm^{-2} \cdot s^{-1} \cdot nm^{-1}$	**Source**
0	1	4730	108248	α^1 Cru	12 26 35.9	−63.09917	B0	1.33	59,654	25,450	SPICAM, SPICAV
1	0	5267	122451	β Cen	14 03 49.4	−60.37305	B1	0.61	56,049	27,947	SPICAM, SPICAV
2	2	5056	116658	α Vir	13 25 11.6	−11.16139	B1	0.98	39,972	18,965	SPICAM, SPICAV
3	4	4853	111123	β Cru	12 47 43.2	−59.68861	B0	1.25	30,544	16,794	SPICAM, SPICAV
4	5	1852	36486	δ Ori	05 32 00.4	−0.29917	O9	2.23	21,670	14,141	SPICAM, SPICAV
5	6	3206	68243	γ^1 Vel	08 09 29.3	−47.34583	B1	4.27	21,209	11,075	SPICAM, SPICAV
6	9	472	10144	α Eri	01 37 42.9	−57.23667	B3	0.46	20,751	9,864	SPICAM
7	14	6527	158926	λ Sco	17 33 36.5	−37.10389	B2	1.63	19,263	7,788	SPICAM, SPICAV
8	8	3165	66811	ζ Pup	08 03 35.1	−40.00333	O5	2.25	18,178	9,992	SPICAM, SPICAV
9	3	2618	52089	ϵ CMa	06 58 37.5	−28.97222	B2	1.50	17,621	17,641	SPICAM, SPICAV, IUE (> 280 nm)
10	12	1948	37742	ζ Ori	05 40 45.5	−1.94278	O9	2.05	16,785	8,667	SPICAM, SPICAV
11	7	2294	44743	β CMa	06 22 42.0	−17.95583	B1	1.98	15,626	10,077	SPICAM, SPICAV
12	13	2491	48915	α CMa	06 45 08.9	−16.71611	A1	−1.46	14,686	7,860	SPICAM, SPICAV
13	10	1790	35468	γ Ori	05 25 07.9	6.34972	B2	1.64	14,501	9,294	SPICAM, SPICAV
14	15	1903	37128	ϵ Ori	05 36 12.8	−1.20194	B0	1.70	13,968	6,663	SPICAM
15	17	6165	149438	τ Sco	16 35 53.0	−28.21611	B0	2.82	12,014	5,515	SPICAM, SPICAV
16	29	5132	118716	ϵ Cen	13 39 53.2	−53.46639	B1	2.30	11,221	4,094	SPICAM, SPICAV
17	28	5231	121263	ζ Cen	13 55 32.4	−47.28833	B2	2.55	10,534	4,403	SPICAM, SPICAV
18	19	5953	143275	δ Sco	16 00 20.0	−22.62167	B0	2.32	10,317	4,732	SPICAM, SPICAV
19	27	7790	193924	α Pav	20 25 38.9	−56.73500	B2	1.94	10,210	4,432	SPICAM, SPICAV
20	21	4199	93030	θ Car	10 42 57.4	−64.39444	B0	2.76	9,955	4,628	SPICAM
21	22	7121	175191	σ Sgr	18 55 15.9	−26.29667	B2	2.02	9,589	4,610	SPICAM, SPICAV
22	16	1899	37043	ι Ori	05 35 26.0	−5.91000	O9	2.77	9,487	6,193	SPICAM, SPICAV
23	26	6580	160578	κ Sco	17 42 29.3	−39.03000	B1	2.41	9,333	4,442	SPICAM, SPICAV
24	24	5191	120315	η UMa	13 47 32.4	49.31333	B3	1.86	9,151	4,538	SPICAM
25	18	2004	38771	κ Ori	05 47 45.4	−9.66972	B0	2.06	9,087	5,120	SPICAM, SPICAV

Journal of Geophysical Research: Planets

10.1029/2017JE005466

Table A1 *(continued)*

Rank					Right ascension	Declination			Flux at 150 nm	Flux at 250 nm	
150 nm	250 nm	HR	HD	Name	(hr min s)	(°)	Spectral type	m_V	(photons $cm^{-2}{\cdot}s^{-1}{\cdot}nm^{-1}$)	(photons $cm^{-2}{\cdot}s^{-1}{\cdot}nm^{-1}$	**Source**
26	25	264	5394	γ Cas	00 56 42.5	60.71667	B0	2.47	8,476	4,493	SPICAM, SPICAV, IUE (> 290 nm)
27	11	5469	129056	α Lup	14 41 55.8	−47.38834	B1	2.30	8,102	9,234	SPICAM, SPICAV
28	23	5440	127972	η Cen	14 35 30.4	−42.15778	B1	2.31	7,686	4,606	SPICAM, SPICAV
29	34	1713	34085	β Ori	05 14 32.3	−8.20167	B8	0.12	7,219	3,283	SPICAM, SPICAV
30	33	6508	158408	υ Sco	17 30 45.8	−37.29583	B2	2.69	6,824	3,310	SPICAV
31	35	4621	105435	δ Cen	12 08 21.5	−50.72250	B2	2.60	6,337	3,204	SPICAM
32	36	1220	24760	ϵ Per	03 57 51.2	40.01028	B0	2.89	6,281	3,203	SPICAM, SPICAV, IUE (> 280 nm)
33	32	5944	143018	π Sco	15 58 51.1	−26.11417	B1	2.89	6,273	3,404	SPICAM, SPICAV
34	30	5984	144217	β^1 Sco	16 05 26.2	−19.80556	B1	2.62	6,191	3,736	SPICAV
35	45	3734	81188	κ Vel	09 22 06.8	−55.01083	B2	2.50	6,077	2,575	SPICAM, SPICAV
36	43	39	886	γ Peg	00 13 14.2	15.18361	B2	2.83	5,769	2,724	SPICAM, SPICAV
37	31	5776	138690	γ Lup	15 35 08.5	−41.16695	B2	2.78	5,728	3,461	SPICAM, SPICAV
38	42	8425	209952	α Gru	22 08 14.0	−46.96111	B7	1.74	5,091	2,766	SPICAM
39	41	6247	151890	μ^1 Sco	16 51 52.2	−38.04750	B1	3.08	5,050	2,799	SPICAM and SPICAV
40	38	7001	172167	α Lyr	18 36 56.3	38.78361	A0	0.03	4,660	2,991	SPICAM and SPICAV
41	40	1791	35497	β Tau	05 26 17.5	28.60750	B7	1.65	4,657	2,811	SPICAM and SPICAV
42	39	3982	87901	α Leo	10 08 22.3	11.96722	B7	1.35	4,340	2,956	SPICAM and SPICAV
43	46	5695	136298	δ Lup	15 21 22.3	−40.64750	B1	3.22	4,295	2,388	SPICAM and SPICAV
44	20	5571	132058	β Lup	14 58 31.9	−43.13389	B2	2.68	4,209	4,724	SPICAM, SPICAV, and IUE (>280 nm)
45	48	1931	37468	σ Ori	05 38 44.8	−2.60000	O9	3.81	4,126	2,037	IUE
46	37	4798	109668	α Mus	12 37 11.0	−69.13555	B2	2.69	3,999	3,023	SPICAM, SPICAV, and IUE (>280 nm)
47	47	5190	120307	ν Cen	13 49 30.3	−41.68778	B2	3.41	3,977	2,058	SPICAM
48	49	2282	44402	ζ CMa	06 20 18.8	−30.06333	B2	3.02	3,972	2,021	SPICAM

Journal of Geophysical Research: Planets

10.1029/2017JE005466

Table A1 *(continued)*

Rank					Right ascension	Declination			Flux at 150 nm	Flux at 250 nm	
150 nm	250 nm	HR	HD	Name	(hr min s)	(°)	Spectral type	m_V	(photons $cm^{-2}{\cdot}s^{-1}{\cdot}nm^{-1}$)	(photons $cm^{-2}{\cdot}s^{-1}{\cdot}nm^{-1}$	**Source**
49	44	1879	36861	λ Ori	05 35 08.3	9.93417	O8	3.54	3,803	2,685	IUE
50	51	4656	106490	δ Cru	12 15 08.7	−58.74889	B2	2.80	3,767	1,863	SPICAM, SPICAV, and IUE (>285 nm)
51	52	6453	157056	θ Oph	17 22 00.6	−24.99944	B2	3.27	3,734	1,859	SPICAM
52	58	4844	110879	β Mus	12 46 16.9	−68.10806	B2	3.05	3,711	1,676	SPICAM
53	55	5948	143118	η Lup	16 00 07.3	−38.39695	B2	3.41	3,558	1,762	SPICAV and IUE
54	60	1788	35411	η Ori	05 24 28.6	−2.39694	B1	3.36	3,476	1,616	SPICAV
55	59	6510	158427	α Ara	17 31 50.5	−49.87611	B2	2.95	3,193	1,673	SPICAM and SPICAV
56	66	8238	205021	β Cep	21 28 39.6	70.56084	B1	3.23	3,128	1,388	SPICAM and IUE >280 nm
57	57	6084	147165	σ Sco	16 21 11.3	−25.59278	B1	2.89	3,000	1,701	SPICAM
58	65	6175	149757	ζ Oph	16 37 09.5	−10.56722	O9	2.56	2,972	1,401	SPICAV
59	53	5193	120324	μ Cen	13 49 37.0	−42.47389	B2	3.04	2,941	1,810	SPICAM, SPICAV, and IUE (>280 nm)
60	50	1910	37202	ζ Tau	05 37 38.7	21.1425	B4	3	2,807	1,909	SPICAM, SPICAV
61	56	3468	74575	α Pyx	08 43 35.5	−33.18639	B1	3.68	2,671	1,733	SPICAM and SPICAV
62	67	5576	132200	κ Cen	14 59 09.7	−42.10416	B2	3.13	2,668	1,305	SPICAV
63	68	5708	136504	ϵ Lup	15 22 40.9	−44.68945	B2	3.37	2,666	1,300	SPICAM, SPICAV, and IUE
64	83	1641	32630	η Aur	05 06 30.9	41.23444	B3	3.17	2,497	969	SPICAM and SPICAV
65	64	5248	121743	ϕ Cen	13 58 16.3	−42.10083	B2	3.83	2,424	1,428	SPICAM and SPICAV
66	77	1756	34816	λ Lep	05 19 34.5	−13.17667	B0	4.29	2,388	1,016	SPICAM, SPICAV, and IUE (>280 nm)
67	61	6462	157246	γ Ara	17 25 23.6	−56.3775	B1	3.34	2,372	1,614	SPICAM, SPICAV, and IUE
68	54	15	358	α And	00 08 23.3	29.09056	B8	2.06	2,230	1,791	OAO2
69	75	1855	36512	υ Ori	05 31 55.8	−7.30139	B0	4.62	2,196	1,076	SPICAM
70	105	1893	37020	θ^1 Ori	05 35 15.9	−5.38722	B0	6.73	2,189	703	OAO2

Note. A list with all modern constellation names, including their abbreviation and genitive, can be found at the home page of the International Astronomical Union, https://www.iau.org/public/themes/constellations/.

Acknowledgments
The MAVEN project is supported by NASA through the Mars Exploration Program. The authors thank Aurélie Reberac and Eric Quémerais for the star catalog and Greg Holsclaw for helping accessing the database. The data used in this section are archived in the Planetary Atmospheres Node of the Planetary Data System (PDS); we used version 13. The authors wish to thank two anonymous referees, whose constructive comments helped to improve the paper.

References

Angelats i Coll, M., Forget, F., López-Valverde, M., & González-Galindo, F. (2005). The first Mars thermospheric general circulation model: The Martian atmosphere from the ground to 240 km. *Geophysical Research Letters*, *32*, L04201. https://doi.org/10.1029/2004GL021368

Angelats i Coll, M., Forget, F., López-Valverde, M. A., Read, P. L., & Lewis, S. R. (2004). Upper atmosphere of Mars up to 120 km: Mars Global Surveyor accelerometer data analysis with the LMD general circulation model. *Journal of Geophysical Research*, *109*, E01011. https://doi.org/10.1029/2003JE002163

Archer, L. E., Stark, G., Smith, P. L., Lyons, J. R., de Oliveira, N., Nahon, L., et al. (2013). Room temperature photoabsorption cross section measurements of CO_2 between 91,000 and 115,000 cm^{-1}. *Journal of Quantitative Spectroscopy and Radiative Transfer*, *117*, 88–92.

Barker, E. S. (1972). Detection of molecular oxygen in the Martian atmosphere. *Nature*, *238*(5), 447–448.

Carleton, N. P., & Traub, W. A. (1972). Detection of molecular oxygen on Mars. *Science*, *177*(4053), 988–992.

Clancy, R. T., & Sandor, B. J. (1998). CO_2 ice clouds in the upper atmosphere of Mars. *Geophysical Research Letters*, *25*, 489–492. https://doi.org/10.1029/98GL00114

Clancy, R. T., Wolff, M. J., James, P. B., Smith, E., Billawala, Y. N., Lee, S. W., & Callan, M. (1996). Mars ozone measurements near the 1995 aphelion: Hubble Space Telescope ultraviolet spectroscopy with the faint object spectrograph. *Journal of Geophysical Research*, *101*(E5), 12,777–12,783.

Clancy, R. T., Wolff, M. J., Lefèvre, F., Cantor, B. A., Malin, M. C., & Smith, M. D. (2016). Daily global mapping of Mars ozone column abundances with MARCI UV band imaging. *Icarus*, *266*, 112–133.

Dubovik, O., Smirnov, A., Holben, B. N., King, M. D., Kaufman, Y. J., Eck, T. F., & Slutsker, I. (2000). Accuracy assessments of aerosol optical properties retrieved from Aerosol Robotic Network (AERONET) Sun and sky radiance measurements. *Journal of Geophysical Research: Atmospheres*, *105*(D), 9791–9806.

England, S. L., Liu, G., Withers, P., Yiğit, E., Lo, D. Y., Jain, S. K., et al. (2016). Simultaneous observations of atmospheric tides from combined in situ and remote observations at Mars from the MAVEN spacecraft. *Journal of Geophysical Research: Planets*, *121*, 594–607. https://doi.org/10.1002/2016JE004997

Fally, S. A. C., Carleer, M., Hermans, C., Jenouvrier, A., Mérienne, M. F., Coquart, B., & Colin, R. (2000). Vandaele Fourier transform spectroscopy of the O_2 Herzberg bands. III. Absorption cross sections of the collision-induced bands and of the Herzberg continuum. *Journal of Molecular Spectroscopy*, *204*(1), 10–20.

Forbes, J. M., Bridger, A. F. C., Bougher, S. W., Hagan, M. E., Hollingsworth, J. L., Keating, G. M., & Murphy, J. (2002). Nonmigrating tides in the thermosphere of Mars. *Journal of Geophysical Research*, *107*(E11), 5113. https://doi.org/10.1029/2001JE001582

Forbes, J. M., & Hagan, M. E. (2000). Diurnal Kelvin wave in the atmosphere of Mars: Towards an understanding of "stationary" density structures observed by the MGS accelerometer. *Geophysical Research Letters*, *27*(2), 3563–3566.

Forget, F., Hourdin, F., Fournier, R., Hourdin, C., Talagrand, O., Collins, M., et al. (1999). Improved general circulation models of the Martian atmosphere from the surface to above 80 km. *Journal of Geophysical Research*, *104*, 24,155–24,176.

Forget, F., Montmessin, F., Bertaux, J.-L., González-Galindo, F., Lebonnois, S., Reberac, A., et al. (2009). Density and temperatures of the upper Martian atmosphere measured by stellar occultations with Mars Express SPICAM. *Journal of Geophysical Research*, *114*, E01004. https://doi.org/10.1029/2008JE003086

González-Galindo, F., Forget, F., López-Valverde, M. A., Angelats i Coll, M., & Millour, E. (2009). A ground-to-exosphere Martian general circulation model: 1. Seasonal, diurnal, and solar cycle variation of thermospheric temperatures. *Journal of Geophysical Research*, *114*, E04001.

González-Galindo, F., López-Valverde, M. A., Forget, F., García-Comas, M., Millour, E., & Montabone, L. (2015). Variability of the Martian thermosphere during eight Martian years as simulated by a ground-to-exosphere global circulation model. *Journal of Geophysical Research: Planets*, *120*, 2020–2035. https://doi.org/10.1002/2015JE004925

Gröller, H., Yelle, R. V., Koskinen, T. T., Montmessin, F., Lacombe, G., Schneider, N. M., et al. (2015). Probing the Martian atmosphere with MAVEN/IUVS stellar occultations. *Geophysical Research Letters*, *42*, 9064–9070. https://doi.org/10.1002/2015GL065294

Hartogh, P., Jarchow, C., Lellouch, E., de Val-Borro, M., Rengel, M., Moreno, R., et al. (2010). Herschel/HIFI observations of Mars: First detection of O_2 at submillimetre wavelengths and upper limits on HCl and H_2O_2. *Astronomy and Astrophysics*, *521*(L49), 1–5.

Huestis, D. L., & Berkowitz, J. (2011). Critical evaluation of the photoabsorption cross section of CO_2 from 0.125 to 201.6 nm at room temperature. *Advances in Geosciences*, *25*, 229–242.

Ityaksov, D., Linnartz, H., & Ubachs, W. (2008). Deep-UV absorption and Rayleigh scattering of carbon dioxide. *Chemical Physics Letters*, *462*(1-3), 31–34.

Jakosky, B. M., Lin, R. P., Grebowsky, J. M., Luhmann, J. G., Mitchell, D. F., Beutelschies, G., et al. (2015). The Mars Atmosphere and Volatile Evolution (MAVEN) mission. *Space Science Reviews*, *195*(1-4), 21–48.

Jakosky, B. M., Slipski, M., Benna, M., Mahaffy, P., Elrod, M., Yelle, R. V., et al. (2017). Mars' atmospheric history derived from upper-atmosphere measurements of $^{38}Ar/^{36}Ar$. *Science*, *355*(6), 1408–1410.

Joshi, M. M., Hollingsworth, J. L., Haberle, R. M., & Bridger, A. F. C. (2000). An interpretation of Martian thermospheric waves based on analysis of a general circulation model. *Geophysical Research Letters*, *27*(5), 613–616.

Keating, G. M., Bougher, S. W., Zurek, R. W., Tolson, R., Cancro, G., Noll, S., et al. (1998). The structure of the upper atmosphere of Mars: In situ accelerometer measurements from Mars Global Surveyor. *Science*, *279*(5357), 1672–1676.

Lebonnois, S, Quémerais, E., Montmessin, F., Lefèvre, F., Perrier, S., Bertaux, J.-L., & Forget, F. (2006). Vertical distribution of ozone on Mars as measured by SPICAM/Mars Express using stellar occultations. *Journal of Geophysical Research*, *111*, E09S05. https://doi.org/10.1029/2005JE002643

Lefèvre, F., Bertaux, J.-L., Clancy, R. T., Encrenaz, T., Fast, K., Forget, F., et al. (2008). Heterogeneous chemistry in the atmosphere of Mars. *Nature*, *454*(7207), 971–975.

Lefèvre, F, & Krasnopolsky, V. (2017). Atmospheric photochemistry. In R. Haberle, et al. (Eds.), *The atmosphere and climate of Mars, Cambridge Planetary Science* (pp. 405–432). UK: Cambridge University Press. https://doi.org/10.1017/9781139060172.013

Lefèvre, F., Lebonnois, S., Montmessin, F., & Forget, F. (2004). Three-dimensional modeling of ozone on Mars. *Journal of Geophysical Research*, *109*, E07004. https://doi.org/10.1029/2004JE002268

Listowski, C., Määttänen, A., Montmessin, F., Spiga, A., & Lefèvre, F. (2014). Modeling the microphysics of CO_2 ice clouds within wave-induced cold pockets in the Martian mesosphere. *Icarus*, *237*, 239–261. https://doi.org/10.1016/j.icarus.2014.04.022

Lo, D. Y., Yelle, R. V., Schneider, N. M., Jain, S. K., Stewart, A. I. F., England, S. L., et al. (2015). Nonmigrating tides in the Martian atmosphere as observed by MAVEN IUVS. *Geophysical Research Letters*, *42*, 9057–9063. https://doi.org/10.1002/2015GL066268

Lu, H. C., Chen, H. K., Chen, H. F., Cheng, B. M., & Ogilvie, J. F. (2010). Absorption cross section of molecular oxygen in the transition $E^3\Sigma_u^- v = 0 - X^3\Sigma_g^- v = 0$ at 38 K. *Astronomy and Astrophysics*, *520*, A19. https://doi.org/10.1051/0004-6361/201013998

Määttänen, A., Montmessin, F., Gondet, B., Scholten, F., Hoffmann, H., González-Galindo, F., et al. (2010). Mapping the mesospheric CO_2 clouds on Mars: MEx/OMEGA and MEx/HRSC observations and challenges for atmospheric models. *Icarus*, *209*, 452–469. https://doi.org/10.1016/j.icarus.2010.05.017

Mahaffy, P. R., Webster, C. R., Atreya, S. K., Franz, H., Wong, M., Conrad, P. G., et al. (2013). Abundance and isotopic composition of gases in the Martian atmosphere from the Curiosity rover. *Science*, *341*(6), 263–266.

Mason, N. J., Gingell, J. M., Davies, J. A., Zhao, H., Walker, I. C., & Siggel, M. R. F. (1996). VUV optical absorption and electron energy-loss spectroscopy of ozone. *Journal of Physics B: Atomic, Molecular and Optical Physics*, *29*(14), 3075–3089.

Matsunaga, F. M., & Watanabe, K. (1967). Total and photoionization coefficients and dissociation continua of O_2 in the 580–1070 Åregion. *Science of Light*, *16*, 31–42.

McClintock, W. E., Schneider, N. M., Holsclaw, G. M., Clarke, J. T., Hoskins, A. C., Stewart, I., et al. (2015). The Imaging Ultraviolet Spectrograph (IUVS) for the MAVEN mission. *Space Science Reviews*, *195*(1), 75–124.

McDunn, T. L., Bougher, S. W., Murphy, J., Smith, M. D., Forget, F., Bertaux, J.-L., & Montmessin, F. (2010). Simulating the density and thermal structure of the middle atmosphere (80–130 km) of Mars using the MGCM-MTGCM: A comparison with MEX/SPICAM observations. *Icarus*, *206*(1), 5–17.

Medvedev, A. S., González-Galindo, F., Yiğit, E., Feofilov, A. G., Forget, F., & Hartogh, P. (2015). Cooling of the Martian thermosphere by CO_2 radiation and gravity waves: An intercomparison study with two general circulation models. *Journal of Geophysical Research: Planets*, *120*, 913–927. https://doi.org/10.1002/2015JE004802

Medvedev, A. S., Nakagawa, H., Mockel, C., Yiğit, E., Kuroda, T., Hartogh, P., et al. (2016). Comparison of the Martian thermospheric density and temperature from IUVS/MAVEN data and general circulation modeling. *Geophysical Research Letters*, *43*, 3095–3104. https://doi.org/10.1002/2016GL068388

Medvedev, A. S., & Yiğit, E. (2012). Thermal effects of internal gravity waves in the Martian upper atmosphere. *Geophysical Research Letters*, *39*, L05201. https://doi.org/10.1029/2012GL050852

Medvedev, A. S., Yiğit, E., Hartogh, P., & Becker, E. (2011). Influence of gravity waves on the Martian atmosphere: General circulation modeling. *Journal of Geophysical Research*, *116*, E10004. https://doi.org/10.1029/2011JE003848

Millour, E., Forget, F., Spiga, A., Navarro, T., Madeleine, J. B., Pottier, A., et al. (2014). A new Mars Climate Database v5.1. In *The Fifth International Workshop on the Mars Atmosphere: Modelling and Observation* (pp. 1301).

Minschwaner, K., Anderson, G. P., Hall, L. A., & Yoshino, K. (1992). Polynomial coefficients for calculating O_2 Schumann-Runge cross sections at 0.5 cm^{-1} resolution. *Journal of Geophysical Research*, *97*(D9), 10103.

Montmessin, F., Bertaux, J.-L., Quémerais, E., Korablev, O., Rannou, P., Forget, F., et al. (2006). Subvisible CO_2 ice clouds detected in the mesosphere of Mars. *Icarus*, *183*(2), 403–410.

Montmessin, F., Korablev, O., Lefèvre, F., Bertaux, J.-L., Fedorova, A., Trokhimovskiy, A., et al. (2017). SPICAM on Mars Express: A 10 year in-depth survey of the Martian atmosphere. *Icarus*, *297*, 195–216. https://doi.org/10.1016/j.icarus.2017.06.022

Montmessin, F., Quémerais, E., Bertaux, J.-L., Korablev, O., Rannou, P., & Lebonnois, S. (2006). Stellar occultations at UV wavelengths by the SPICAM instrument: Retrieval and analysis of Martian haze profiles. *Journal of Geophysical Research*, *111*, E09S09. https://doi.org/10.1029/2005JE002662

Moudden, Y., & Forbes, J. M. (2008). Topographic connections with density waves in Mars' aerobraking regime. *Journal of Geophysical Research*, *113*, E11009. https://doi.org/10.1029/2008JE003107

Nier, A. O., & McElroy, M. B. (1977). Composition and structure of Mars' upper atmosphere—Results from the neutral mass spectrometers on Viking 1 and 2. *Journal of Geophysical Research*, *82*(28), 4341–4349.

Ogawa, M., & Cook, G. R. (1958). Absorption coefficients of O_3 in the vacuum ultraviolet region. *The Journal of Chemical Physics*, *28*(1), 173–174.

Ogawa, S., & Ogawa, M. (1975). Absorption cross sections of $O_2(a^1\Delta_g)$ and $O_2(X^3\Sigma_g^-)$ in the region from 1087 to 1700 Å. *Canadian Journal of Physics*, *53*(19), 1845–1852.

Parkinson, W. H., Rufus, J., & Yoshino, K. (2003). Absolute absorption cross section measurements of in the wavelength region 163–200 nm and the temperature dependence. *Chemical Physics*, *290*(2-3), 251–256.

Perrier, S., Bertaux, J.-L., Lefèvre, F., Lebonnois, S., Korablev, O., Fedorova, A., & Montmessin, F. (2006). Global distribution of total ozone on Mars from SPICAM/MEX UV measurements. *Journal of Geophysical Research*, *111*, E09S06. https://doi.org/10.1029/2006JE002681

Perryman, M. A. C., Lindegren, L., Kovalevsky, J., Hoeg, E., Bastian, U., Bernacca, P. L., et al. (1997). The HIPPARCOS catalogue. *Astronomy and Astrophysics*, *323*, L49–L52.

Quémerais, E., Bertaux, J.-L., Korablev, O., Dimarellis, E., Cot, C., Sandel, B. R., & Fussen, D. (2006). Stellar occultations observed by SPICAM on Mars Express. *Journal of Geophysical Research*, *111*, E09S04. https://doi.org/10.1029/2005JE002604

Sandel, B. R., Gröller, H., Yelle, R. V., Koskinen, T. T., Lewis, N. K., Bertaux, J.-L., et al. (2015). Altitude profiles of O_2 on Mars from SPICAM stellar occultations. *Icarus*, *252*, 154–160.

Serdyuchenko, A., Gorshelev, V., Weber, M., Chehade, W., & Burrows, J. P. (2014). High spectral resolution ozone absorption cross-sections—Part 2: Temperature dependence. *Atmospheric Measurement Techniques*, *7*(2), 625–636.

Smith, M. D., Wolff, M. J., Spanovich, N., Ghosh, A., Banfield, D., Christensen, P. R., et al. (2006). One Martian year of atmospheric observations using MER Mini-TES. *Journal of Geophysical Research*, *111*, E12S13. https://doi.org/10.1029/2006JE002770

Snow, M., Reberac, A., Clarke, J. T., McClintock, W. E., & Woods, T. N. (2013). A new catalog of ultraviolet stellar spectra for calibration, *Cross-calibration of far UV spectra of solar system objects and the heliosphere* (pp. 191–226). New York: Springer.

Snowden, D., Yelle, R. V., Cui, J., Wahlund, J. E., Edberg, N. J. T., & Ågren, K. (2013). The thermal structure of Titan's upper atmosphere, I: Temperature profiles from Cassini INMS observations. *Icarus*, *226*(1), 552–582.

Spiga, A., González-Galindo, F., López-Valverde, M. A., & Forget, F. (2012). Gravity waves, cold pockets and CO_2 clouds in the Martian mesosphere. *Geophysical Research Letters*, *39*, L02201. https://doi.org/10.1029/2011GL050343

Stark, G., Yoshino, K., Smith, P. L., & Ito, K. (2007). Photoabsorption cross section measurements of CO_2 between 106.1 and 118.7 nm at 295 and 195 K. *Journal of Quantitative Spectroscopy and Radiative Transfer*, *103*(1), 67–73.

Tikhonov, A. N., & Arsenin, V. Y. (1977). *Solutions of ill-posed problems*. Washington, DC: V. H. Winston.

Trauger, J. T., & Lunine, J. I. (1983). Spectroscopy of molecular oxygen in the atmospheres of Venus and Mars. *Icarus*, *55*, 272–281.

Twomey, S. (1977). Some aspects of the inversion problem in remote sensing.

Viereck, R. A., & Puga, L. C. (1999). The NOAA Mg II core-to-wing solar index: Construction of a 20-year time series of chromospheric variability from multiple satellites. *Journal of Geophysical Research*, *104*(A5), 9995–10,005.

Viereck, R., Puga, L., McMullin, D., Judge, D., Weber, M., & Tobiska, W. K. (2001). The Mg II index: A proxy for solar EUV. *Geophysical Research Letters*, *28*(7), 1343–1346. https://doi.org/10.1029/2000GL012551

Walterscheid, R. L. (1981). Dynamical cooling induced by dissipating internal gravity waves. *Geophysical Research Letters*, *8*, 1235–1238. https://doi.org/10.1029/GL008i012p01235

Wilson, R. J. (2002). Evidence for nonmigrating thermal tides in the Mars upper atmosphere from the Mars Global Surveyor Accelerometer Experiment. *Geophysical Research Letters*, *29*(7), 1120. https://doi.org/10.1029/2001GL013975

Withers, P., Pratt, R., Bertaux, J.-L., & Montmessin, F. (2011). Observations of thermal tides in the middle atmosphere of Mars by the SPICAM instrument. *Journal of Geophysical Research*, *116*, E11005. https://doi.org/10.1029/2011JE003847

Wu, C. Y. R., Judge, D. L., & Matsui, T. (2005). High-temperature ultrahigh-resolution absorption cross-section measurements of O_2 in the EUV region. *Journal of Electron Spectroscopy and Related Phenomena*, *144-147*, 123–126.

Yiğit, E., & Medvedev, A. S. (2009). Heating and cooling of the thermosphere by internal gravity waves. *Geophysical Research Letters*, *36*, L14807. https://doi.org/10.1029/2009GL038507

Yiğit, E., Medvedev, A. S., & Hartogh, P. (2015). Gravity waves and high-altitude CO_2 ice cloud formation in the Martian atmosphere. *Geophysical Research Letters*, *42*, 4294–4300. https://doi.org/10.1002/2015GL064275

Yoshino, K., Cheung, A. S. C., Esmond, J. R., Parkinson, W. H., Freeman, D. E., Guberman, S. L., et al. (1988). Improved absorption cross-sections of oxygen in the wavelength region 205–240 nm of the Herzberg continuum. *Planetary and Space Science*, *36*(12), 1469–1475.

Yoshino, K., Esmond, J. R., Freeman, D. E., & Parkinson, W. H. (1993). Measurements of absolute absorption cross sections of ozone in the 185-to 254-nm wavelength region and the temperature dependence. *Journal of Geophysical Research*, *98*(D3), 5205–5211.

Yoshino, K., Parkinson, W. H., Ito, K., & Matsui, T. (2005). Absolute absorption cross-section measurements of Schumann-Runge continuum of O_2 at 90 and 295 K. *Journal of Molecular Spectroscopy*, *229*(2), 238–243.

Yoshino, K., Sun, Y., Esmond, J. R., Parkinson, W. H., Ito, K., & Matsui, T. (1996). Absorption cross section measurements of carbon dioxide in the wavelength region 118.7–175.5 nm and the temperature dependence. *Journal of Quantitative Spectroscopy and Radiative Transfer*, *55*(1), 53–60.